Check for updates

AUTOIMMUNITY

Copyright © 2025 The Authors, some rights reserved; exclusive licensee American Association for the Advancement of Science. No claim to original U.S. Government Works

Epidermal ZBP1 stabilizes mitochondrial Z-DNA to drive UV-induced IFN signaling in autoimmune photosensitivity

Benjamin Klein[1]*, Mack B. Reynolds[2], Bin Xu[1], Mehrnaz Gharaee-Kermani[1,3], Yiqing Gao[1], Celine C. Berthier[4], Svenja Henning[1], Lam C. Tsoi[3,5,6], Shannon N. Loftus[1], Kelsey E. McNeely[1], Christine M. Goudsmit[7], Amanda M. Victory[1], Craig Dobry[3], Grace A. Hile[3], Feiyang Ma[1,3], Jessica L. Turnier[7], Johann E. Gudjonsson[1,3], Mary X. O'Riordan[2], J. Michelle Kahlenberg[1,3]*

Photosensitivity is observed in numerous autoimmune diseases and drives poor quality of life and disease flares. Elevated epidermal type I interferon (IFN) production primes for photosensitivity and enhanced inflammation, but the substrates that sustain and amplify this cycle remain undefined. We show that IFN-induced Z-DNA binding protein 1 (ZBP1) stabilizes ultraviolet (UV) B–induced cytosolic Z-DNA derived from oxidized mitochondrial DNA. ZBP1 is up-regulated in the epidermis of adult and pediatric patients with autoimmune photosensitivity. In patient-derived samples, lupus keratinocytes accumulate extensive cytosolic Z-DNA after UVB exposure, and transfection of keratinocytes with Z-DNA results in stronger IFN production through cyclic guanosine monophosphate–adenosine monophosphate synthase–stimulator of interferon genes (cGAS-STING) activation compared with the more conventional B-DNA. ZBP1 knockdown abrogates UVB-induced IFN responses, whereas overexpression results in a lupus-like phenotype with spontaneous Z-DNA accumulation and IFN production. Our results highlight Z-DNA and ZBP1 as critical mediators for UVB-induced inflammation and uncover how type I IFNs prime for cutaneous inflammation in photosensitivity.

INTRODUCTION

Autoimmune photosensitivity is seen in type I interferon (IFN)–driven skin diseases such as systemic (SLE) and cutaneous lupus erythematosus (CLE) as well as dermatomyositis (DM) (*1*–*4*). Up to 81% of patients with SLE and CLE are affected by photosensitivity, defined by severe skin reactions to brief ultraviolet (UV) light exposure. Photosensitivity leads to poor quality of life for patients (*1*, *5*), and in SLE, UV light can also trigger systemic inflammation, including nephritis (*1*, *6*–*8*). Therapies to prevent photosensitivity are limited to sunscreen use, for which compliance is low (*9*).

The skin is the most commonly affected organ of patients with lupus (*10*). Nonlesional skin of patients at risk for lupus exhibits robust IFN secretion even with minimal IFN signature in the blood (*10*–*12*). This cutaneous type I IFN production leads to increased epidermal cell death (*3*) and inflammatory activation of myeloid cells (*12*) and is widely accepted as a driver of CLE and DM lesions (*3*, *11*, *13*, *14*). Within the skin, basal keratinocytes (KCs) are the main target of UVB irradiation and are major contributors to the IFN signature observed in these diseases through chronic secretion of IFN kappa (IFN-κ) (*3*, *15*, *16*). Similar to type I IFNs, type III IFNs (composed of IFNλ 1 to 4) are up-regulated in CLE skin and may also affect inflammatory responses in photosensitivity (*17*, *18*). It is assumed that the IFN signature in nonlesional skin of patients with lupus enhances immune activation and thus contributes to the transition to lesional skin or even systemic disease after environmental triggers, such as UV light (*11*). However, the precise mechanism by which a cutaneous type I IFN–rich environment accelerates inflammation after UV light has not been identified.

The effects of UV light in KCs include mitochondrial DNA (mtDNA) damage, mitochondrial fragmentation, and release of mtDNA into the cytoplasm (*19*–*21*). UV light is mainly absorbed by complex I of the mitochondrial electron transport chain and leads to reactive oxygen species (ROS) accumulation and disruption of respiratory chain complexes (*22*). MtDNA is especially susceptible to UV-induced damage because it is located in the inner mitochondrial matrix in close proximity to produced ROS (*19*). UV light causes type I IFN responses in the skin, which is accelerated in autoimmune photosensitivity (*1*, *2*, *23*). It has been proposed that this IFN stems from cytoplasmic nucleic acids that activate innate immune sensors. Despite growing evidence that this happens in a cyclic guanosine 5′-monophosphate–adenosine 5′-monophosphate synthase (cGAS) stimulator of interferon genes (STING)–dependent fashion (*24*, *25*), the substrate of cGAS activation after UV exposure has not been identified.

MtDNA induces type I IFN responses in multiple autoimmune diseases, including SLE (*26*–*30*). Specifically, oxidized mtDNA is highly interferogenic in lupus neutrophils (*28*, *29*). Moreover, mtDNA derived from mitochondria-containing red blood cells activates IFN responses in lupus monocytes contributing to the IFN signature observed in SLE blood (*31*).

Mitochondrial dysfunction can lead to liberation of mtDNA into the cytoplasm (*27*, *32*, *33*). After release of mtDNA, multiple pattern recognition receptors (PRRs), including absent in melanoma 2 (AIM2),

[1]Division of Rheumatology, Department of Internal Medicine, University of Michigan, Ann Arbor, MI, USA. [2]Department of Microbiology and Immunology, University of Michigan, Ann Arbor, MI, USA. [3]Department of Dermatology, University of Michigan, Ann Arbor, MI, USA. [4]Division of Nephrology, Department of Internal Medicine, University of Michigan, Ann Arbor, MI, USA. [5]Department of Biostatistics, University of Michigan, Ann Arbor, MI, USA. [6]Department of Computational Medicine and Bioinformatics, University of Michigan, Ann Arbor, MI, USA. [7]Division of Pediatric Rheumatology, Department of Pediatrics, University of Michigan, Ann Arbor, MI, USA. *Corresponding author. Email: benjamk@med.umich.edu (B.K.); mkahlenb@med.umich.edu (M.K.)

Downloaded from https://www.science.org at University of Michigan Ann Arbor on March 07, 2025

cGAS, and Z-DNA binding protein 1 (ZBP1), can be activated (*26*, *32*–*34*). ZBP1 itself is an IFN-induced gene and senses nucleic acids in Z conformation with its Zα domain to provide antiviral defense (*35*–*39*). In contrast with B-DNA, left-handed Z-DNA is more prone to occur in GC-rich sequences and is characterized by a zig-zag–shaped backbone. This DNA conformation is induced by high-salt conditions, torsional stress, oxidized bases such as 8-oxo-2′-deoxyguanosine (8-oxodG), or other base modifications and further stabilized by Z-DNA binding proteins (*35*, *40*, *41*). MtDNA can undergo Z-DNA formation upon oxidation, mitochondrial genome instability, and negative supercoiling (*34*). Mitochondrial-derived Z-DNA is detected by ZBP1 and cGAS to sustain type I IFN responses in cardiomyocytes to promote doxorubicin-induced cardiotoxicity (*34*).

Given that it is known that mitochondrial damage occurs after UV light exposure and that the type I IFN signature is linked to autoimmune photosensitive diseases, we hypothesized that UV exposure could lead to oxidized mitochondria-derived cytosolic Z-DNA accumulation that is stabilized by type I IFN–induced up-regulation of ZBP1. This combination of Z-DNA accumulation and increased ZBP1 would then lead to robust type I IFN responses in KCs.

Here, we show that UV-induced Z-DNA formation derives from oxidized mtDNA in human KCs. Furthermore, we demonstrate that epidermal ZBP1 is up-regulated in nonlesional and lesional skin of patients with SLE and DM. We provide evidence of enhanced ZBP1-stabilized Z-DNA accumulation in an IFN-rich environment, which further sustains IFN signaling in KCs after UV exposure via cGAS-STING activation. Z-DNA is more immunostimulatory than B-DNA and depends on recognition by cGAS and subsequent STING signaling. Knockdown of ZBP1 in KCs attenuates type I IFN and IFN-stimulated gene (ISG) expression after UV, and overexpression of ZBP1 in KCs results in enhanced cytosolic Z-DNA retention and type I IFN signaling. Together, our data identify a pathway that explains how an IFN-rich environment primes the skin for photosensitivity through ZBP1-mediated stabilization of Z-DNA, which drives activation of the cGAS-STING pathway. This has important implications for treatment and prevention of cutaneous and systemic flares of photosensitive autoimmune diseases.

RESULTS

UV irradiation–induced type I and III IFN is dependent on mtROS and mtDNA

UV light was previously shown to cause mitochondrial damage, ROS accumulation, and IFN production (*22*), but how these changes are related to each other has not been well characterized. We hypothesized that UV-induced mitochondrial stress would lead to release of mtDNA followed by IFN production in KCs. To investigate mitochondrial ROS (mtROS) formation, we preincubated N/TERT KCs with or without mitoTEMPO, a mitochondrially targeted antioxidant, and irradiated them with UVB light (Fig. 1A). We observed early increased mtROS formation in KCs 30 min after UVB exposure that was inhibited by mitoTEMPO as measured by mitochondrial superoxide (MitoSOX) red staining (Fig. 1, A and B). Further, the measurement of mitochondrial depolarization after UVB exposure in a time course using a polarization-dependent dye, MitoTrackerDeepRed (MTDR), and a polarization-independent dye, MitoTrackerGreen (MTG), revealed early mitochondrial membrane depolarization in KCs 30 min after UVB, in line with mtROS formation (fig. S1, A to C). We then performed Seahorse assays after UVB stimulation of KCs, which showed a significant global drop of respiratory parameters (Fig. 1C and fig. S1D), in line with mitochondrial stress after UVB exposure. To test whether mtROS promote subsequent type I and III IFN signaling after UV light, we then assessed the effect of mitoTEMPO on type I and III IFN gene expression. Rotenone, a complex I inhibitor and inducer of mtROS (*42*), was used as a positive control. Both UVB and rotenone induced a significant increase in *interferon beta 1* (*IFNB1*) and *interferon lambda 3* (*IFNL3*) expression 6 hours after UVB, which was inhibited by mitoTEMPO (Fig. 1D). MitoTEMPO also dampened the expression of later-expressed IFN-regulated genes—*IFNK*, *2′-5′-oligoadenylate synthetase like* (*OASL*), and *MX dynamin like GTPase 1* (*MX1*)—24 hours after UV exposure (Fig. 1E). These results indicate that mtROS are promoting type I and III IFN responses after UV in KCs. Next, we wanted to investigate whether UVB-induced mitochondrial stress would lead to mtDNA release and whether this would promote type I IFN responses. The measurement of cytosolic fractions via polymerase chain reaction (PCR) revealed increased abundance of mtDNA after UVB exposure (Fig. 1, F and G, and fig. S1E). Given that type I IFNs have been implicated in photosensitive responses and are responsible for an autocrine loop of inflammation upon UV exposure that results in enhanced IFN gene expression (fig. S1F) (*3*, *13*), we then tested whether mtDNA release is increased by preincubation with IFN-α. Strikingly, IFN-α preincubation led to stronger mtDNA abundance in the cytoplasm after UVB, whereas IFN-α priming alone did not increase cytosolic mtDNA significantly (Fig. 1G and fig. S1E). To test whether mtDNA is required for UV-induced type I IFN induction, we then depleted mtDNA selectively with the nucleoside 2′3′-dideoxycytosine (ddC) and observed a significant reduction of mtDNA abundance and type I IFN expression 6 hours after UVB exposure (Fig. 1, H to J, and fig. S1G). Given that cGAS senses mtDNA to promote type I IFN responses (*33*), we next investigated whether cGAS is necessary for UVB-induced IFN signaling. We tested a recently developed, specific inhibitor of cGAS (G140) (*43*) in N/TERTs after double-stranded DNA (dsDNA) transfection and found complete abrogation of type I IFN after transfection at both inhibitor doses tested (fig. S1H), confirming dependence on cGAS. Next, we used this inhibitor before UVB exposure and found that early UVB-induced IFN responses in KCs are also highly dependent on cGAS (fig. S1I), similar to previous murine skin data (*24*). We then wanted to explore the reason for higher abundance of mtDNA after UVB with IFN-α priming and tested whether the increase in cytosolic mtDNA abundance was due to IFN-α–mediated enhancement of ROS formation. Unexpectedly, IFN-α did not increase mtROS or cellular ROS in N/TERTs (Fig. 1K and fig. S1J). Together, these results indicate that mtROS, mtDNA, and cGAS are required for early IFN responses after UVB in KCs.

IFN-α enhances UVB-induced Z-DNA formation derived from mtDNA

We next wanted to investigate what might cause increased abundance of cytoplasmic mtDNA in IFN-α–primed KCs after UVB exposure. Oxidation of DNA and mtDNA instability can lead to formation and stabilization of left-handed Z-DNA (*34*, *40*). Therefore, we assessed Z-DNA localization and accumulation after UV exposure using immunofluorescence microscopy of Z-DNA, the mitochondrial outer membrane protein TOMM20, and 4′,6-diamidino-2-phenylindole (DAPI). Using a Z22 antibody that was confirmed to stain Z-DNA in previous reports (*34*), we screened for enhanced Z-DNA staining and

Downloaded from https://www.science.org at University of Michigan Ann Arbor on March 07, 2025

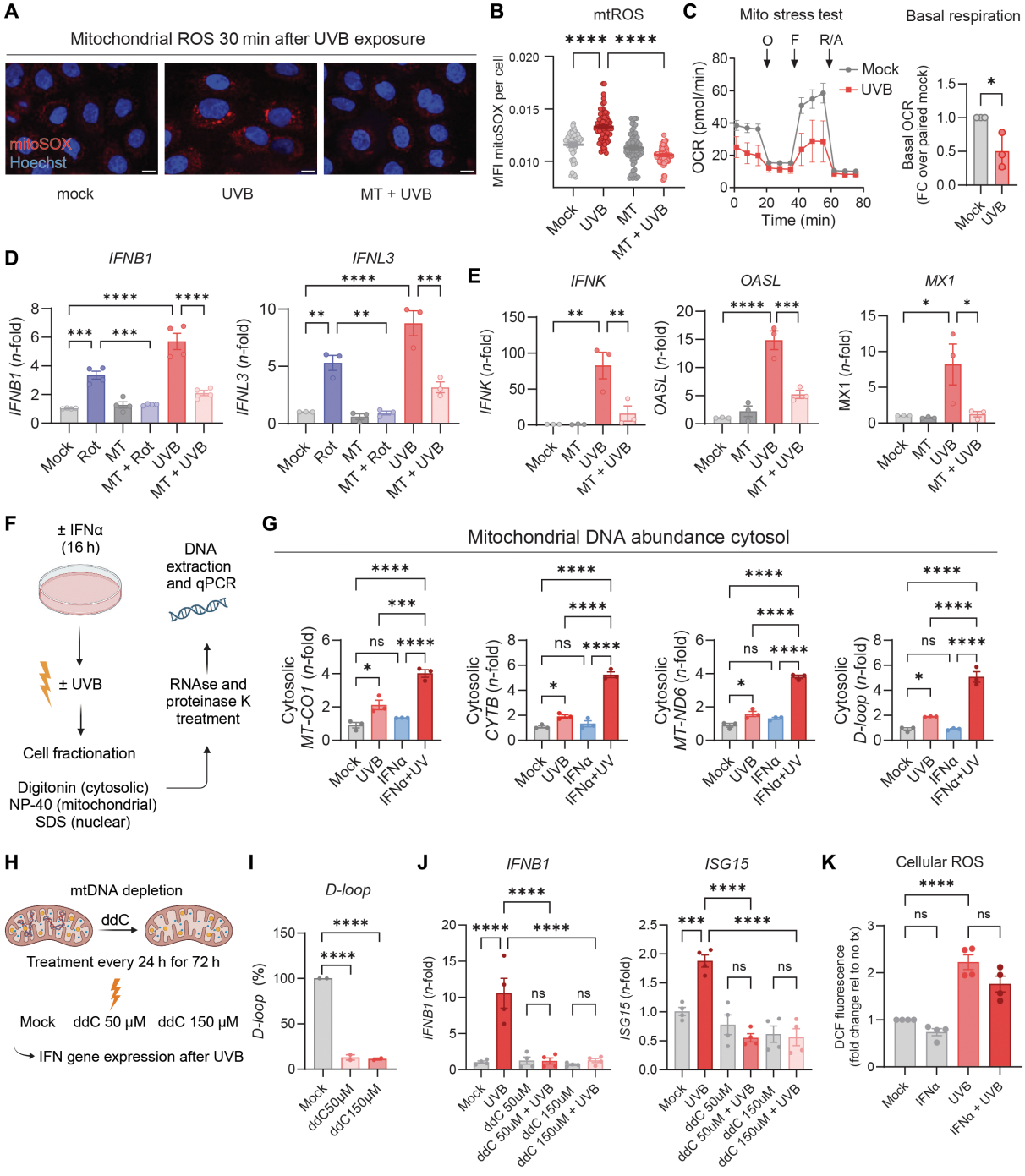


Fig. 1. Early UVB-induced IFN is dependent on release of mtDNA. (**A**) Representative images from N/TERTs treated ± mitoTEMPO (MT) ± UVB irradiation stained with MitoSOX red and Hoechst 33342, scale bar = 10 µm. (**B**) Quantification of MitoSOX intensity per cell using CellProfiler software. (**C**) Seahorse XF analysis of OCR in UVB-irradiated N/TERTs using the Mito Stress Test assay, with additions of oligomycin (O), FCCP, rotenone (R), and antimycin A (A) at indicated time points and comparison of basal OCR with fold change (FC) over paired mock, $n = 3$. (**D**) N/TERTs were treated with rotenone, mitoTEMPO, or UVB for 6 hours. Gene expression of *IFNB1* ($n = 4$) and *IFNL3* ($n = 3$) was determined by qtPCR. (**E**) Gene expression of *IFNK*, *MX1*, and *OASL* ± mitoTEMPO ± UVB 24 hours after UVB exposure ($n = 3$). (**F**) Experimental approach for cytosolic mtDNA extraction after UVB and type I IFN priming. (**G**) Quantification of mtDNA abundance in cytosolic fractions (fold change over nuc*18S* RNA) ($n = 3$). (**H**) Left: Experimental approach for mtDNA depletion in N/TERTs using nucleoside ddC. Treatment with ddC was performed for 72 hours. After irradiation, medium was changed to ddC-free medium until gene expression analysis. (**I**) D-loop abundance normalized to 18*S* rRNA after ddC treatment in WCLs, average of $n = 2$ independent experiments in technical triplicates. (**J**) Quantitative gene expression of *IFNB1* and *ISG15* 6 hours after UVB exposure, data of $n = 2$ independent experiments with technical duplicates. (**K**) Quantification of cellular ROS using the indicator CM-H_2DCFDA, average of three to five replicates per condition related to mock, $n = 4$. Means + SEM. *P* values were calculated using ordinary one-way analysis of variance (ANOVA) followed by Šidák's multiple comparison test or Student's *t* test. $^*P < 0.05$, $^{**}P < 0.01$, $^{***}P < 0.001$, and $^{****}P < 0.0001$. ns, not significant.

Downloaded from https://www.science.org at University of Michigan Ann Arbor on March 07, 2025

accumulation after UVB exposure. Using super-resolved structured illumination microscopy, we observed low baseline staining and mitochondrial localization of Z-DNA without stimulation (Fig. 2, A and B). Strikingly, after UVB, we observed an increase in Z-DNA outside of the mitochondrial compartment with formation of prominent Z-DNA puncta (Fig. 2, C and D). We used a spinning disk confocal microscope to image larger cell numbers after UVB treatment for quantitative analysis and observed strong staining of cytosolic large Z-DNA puncta (Fig. 2E). Automated image analysis confirmed that UVB significantly increased total and cytosolic Z-DNA 3 hours after irradiation, which was abrogated by preincubation with mitoTEMPO (Fig. 2, E to G). Moreover, we observed significantly more mitochondrial fragments after UVB exposure, which was also rescued by mitoTEMPO (Fig. 2H). Z-DNA was localized within the mitochondrial network when cells were preincubated with mitoTEMPO (Fig. 2E), suggesting a stabilization of the mitochondrial network and inhibition of Z-DNA escape to the cytoplasm. We confirmed mitochondrial origin of Z-DNA by the depletion of mtDNA using ddC, which reduced Z-DNA intensity and puncta significantly but did not influence UVB-induced mitochondrial fragmentation (fig. S2, A to C). Because ddC also decreases mitochondrial RNA, we further confirmed Z-DNA origin by proximity ligation assay (PLA) of Z-DNA and B-DNA showing an increased signal for Z-DNA/B-DNA after UVB exposure compared with baseline, indicating that Z-DNA occurs in proximity to B-DNA (fig. S2, D to G).

To explore whether type I IFNs affected UVB-induced cytosolic Z-DNA accumulation, we first treated N/TERTs for 16 hours with IFN-α before irradiation to mimic a chronic type I IFN environment, such as that seen in SLE (*3*, *10*–*12*). After UVB exposure and IFN-α priming, we observed a notable accumulation of cytosolic Z-DNA puncta associated with mitochondrial fragmentation (Fig. 2, E to H). MitoTEMPO fully rescued this phenotype by maintaining the mitochondrial network (Fig. 2, E to H). PLA confirmed an increase in Z-DNA after priming with IFN-α after UVB (fig. S2, D to G). Furthermore, to confirm increased abundance of Z-DNA (but not Z-RNA) after IFN-α-priming and UVB exposure, we treated N/TERTs with deoxyribonuclease I (DNase I) or ribonuclease A (RNase A). Strikingly, we found significant decreases in total DNA and cytosolic Z-DNA puncta after DNase I treatment, whereas RNase A–treated cells exhibited no change in Z-DNA abundance (Fig. 2, I to K). Collectively, these results strongly indicate cytosolic Z-DNA accumulation that is derived from mitochondria upon UV exposure and is markedly increased in a type I IFN–rich environment.

UVB-induced oxidative DNA damage promotes cytosolic Z-DNA accumulation

Given our observations of UVB-induced mtROS and the reduction of Z-DNA by mitoTEMPO, we suspected that UVB-driven oxidative mtDNA lesions would contribute to Z-DNA accumulation. Previous published evidence showed that oxidative damage of guanosine [8-oxo-2′-deoxyguanosine (8oxodG)] promotes Z-DNA formation through energetic favorability, because 8oxodG hinders steric formation of B-DNA and favors Z-DNA formation (*40*). After UV exposure, 8-oxodG staining was diffuse, and costaining with Z-DNA and TOMM20 revealed proximity of large Z-DNA puncta with spots of enhanced 8oxodG damage outside of mitochondria after UVB exposure (Fig. 3, A and B). Moreover, after the combination of IFN-α priming and UVB exposure, we observed that accumulation of large Z-DNA puncta occurred in spots with increased 8oxodG staining (Fig. 3, A to C). 8oxodG staining after UVB exposure was significantly enhanced in the mitochondrial compartment (Fig. 3D) and was significantly reduced by mitoTEMPO (fig. S3, A and B). Furthermore, there was a significant positive correlation of cytosolic Z-DNA puncta and 8oxodG intensity per cell, suggesting that 8oxodG damage promotes Z-DNA conformation (Fig. 3E). Mitochondrial fragmentation also showed a positive correlation with cytosolic Z-DNA accumulation (fig. S3C), suggesting that cytosolic Z-DNA accumulation is associated with mitochondrial damage.

UVB also causes dose-dependent formation of cyclobutane pyrimidine dimers (CPDs) in KCs, which can occur both in mtDNA and nuclear DNA (*44*). Hence, we stained for CPDs and saw significant increases in CPD abundance after our UVB dose that were mostly nuclear and not enhanced with IFN-α priming (fig. S3, D and E). Furthermore, 3 hours after UVB exposure at 50 mJ/cm^2, we did not see micronucleus formation, which have been reported to occur after genotoxic stress as potential substrates for cGAS recognition (fig. S3F) (*45*).

To confirm the cellular origin of Z-DNA after UVB exposure and to test which UVB-induced DNA modification is associated with Z-DNA abundance, we performed PLA with antibodies against 8oxodG/Z-DNA and CPD/Z-DNA (Fig. 3F). Strikingly, we observed strong cytosolic PLA signals in the first antibody combination (8oxodG/Z-DNA) after UVB exposure, whereas CPD/Z-DNA had almost no signal (Fig. 3, F and G). To test whether Z-DNA formation in naked DNA required oxidative lesions, we used an assay that examines Z-DNA formation in poly[deoxyguanylic-deoxycytidylic (dG:dC)] oligos induced by high concentrations of NaCl (*46*, *47*). In this assay, the sodium ions interact with the negatively charged phosphate backbone of the DNA to facilitate the formation of Z-DNA in a dose-dependent fashion. Z-DNA conformation is then measured using the $A_{260/295}$ ratio, which is significantly lower in Z-DNA compared with the B conformation. Z-DNA formation under high-salt conditions was confirmed (Fig. 3H) (*46*, *48*). To test whether UVB exposure itself would directly lead to Z-DNA accumulation, we irradiated poly(dG:dC) with low (50 mJ/cm^2) and high (200 mJ/cm^2) doses of UVB light. We did not observe direct induction of Z-DNA conformation upon UVB exposure at both doses (Fig. 3I), suggesting no direct oxidative DNA damage at the doses used in our in vitro system. However, the induction of oxidation by H_2O_2 permitted Z-DNA formation at significantly lower concentrations of NaCl (Fig. 3J). These results suggest that UVB light promotes Z-DNA conformation indirectly by accumulation of oxidative DNA damage.

ZBP1 is overexpressed in photosensitive autoimmune skin diseases and correlates with type I IFN scores

Because we saw that mitochondrial and cellular ROS are not affected by IFN-α priming, we next wanted to investigate what might lead to enhanced mitochondrial DNA abundance in the Z conformation in an IFN-rich environment. Given that UVB-mediated cytosolic mtDNA in Z form is promoted by type I IFNs (Fig. 2, E to H), we hypothesized that the elevated chronic type I IFN environment in autoimmune photosensitive diseases may contribute to this sustained response. Intriguingly, Z-DNA conformation can be stabilized by the IFN-regulated gene *ZBP1* (*34*–*36*), so we chose to further examine the role of ZBP1 in patients with autoimmune photosensitive diseases (Fig. 4A). *ZBP1* expression was significantly up-regulated in a large cohort of CLE lesional skin biopsies ($n = 90$) compared with those of healthy controls (CTLs) ($n = 13$) (Fig. 4B). This up-regulation

Downloaded from https://www.science.org at University of Michigan Ann Arbor on March 07, 2025

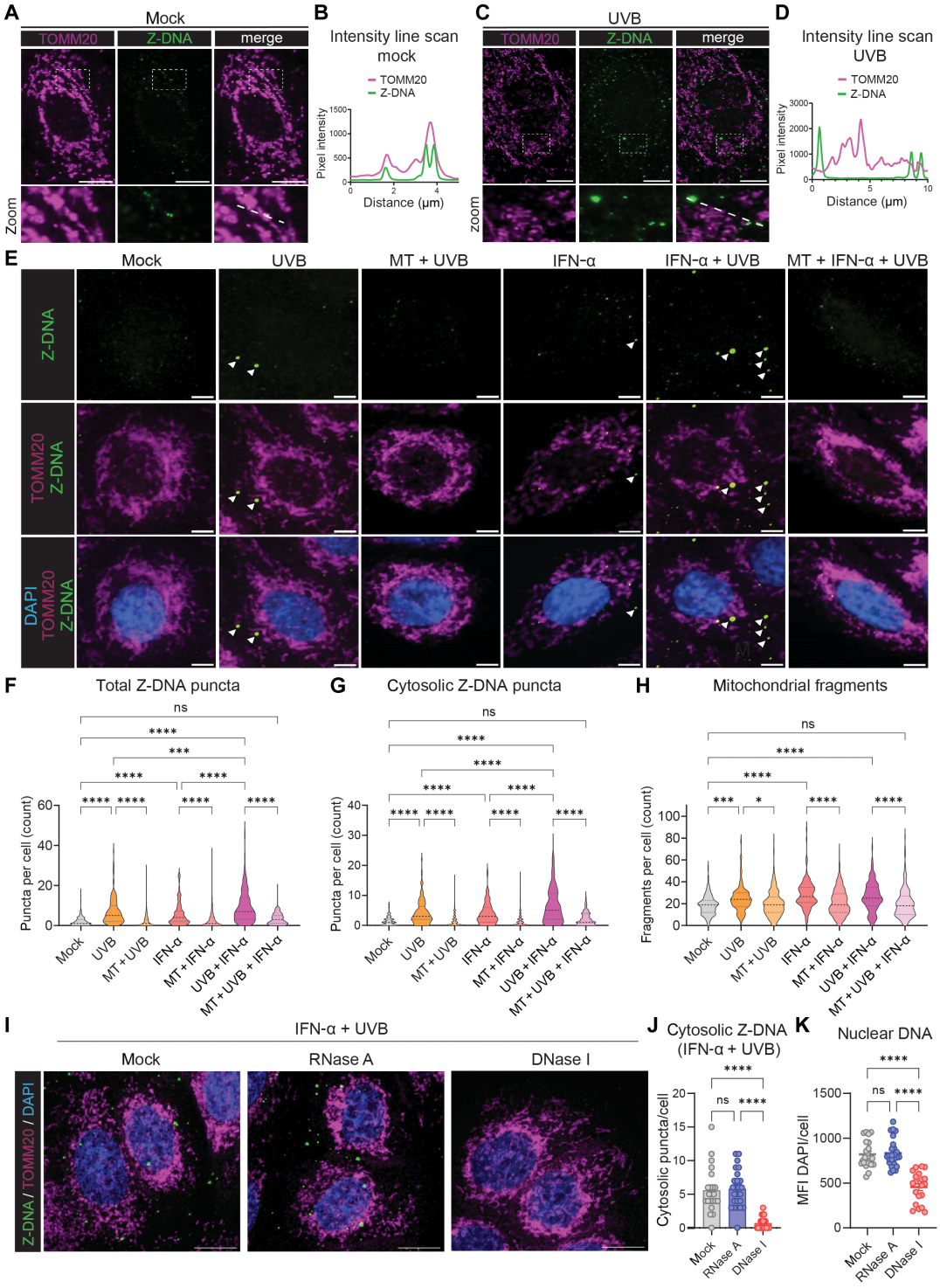


Fig. 2. IFN-α priming increases cytosolic UVB-induced Z-DNA. (**A**) Representative confocal microscopy from N/TERTs of TOMM20, Z-DNA, and DAPI without stimulation. (**B**) Line scan analysis of the line in (F). (**C**) Representative confocal microscopy from N/TERTs of TOMM20 and Z-DNA 3 hours after UVB exposure. (**D**) Line scan analysis of the dotted white line in (H). (**E**) Representative confocal images from N/TERTs of TOMM20, Z-DNA, and DAPI ± mitoTEMPO, pretreatment with IFN-α or 3 hours after UVB. Scale bars, 5 µm. (**F** to **H**) Quantification of Z-DNA puncta (F and G) and mitochondrial fragments (H) (objects < 1 µm^2 with circularity > 0.6) using CellProfiler software, data of $n = 4$ independent experiments. (**I**) Representative confocal images (Z-stacks with maximum intensity projection across 8 µm) of N/TERTs treated with IFN-α and UVB 3 hours after UVB exposure ± RNase A (4 mg/ml) ± DNase I (200 U/ml) stained for Z-DNA, TOMM20, and DAPI. Scale bars, 10 µm. (**J** and **K**) Quantification of cytosolic Z-DNA puncta (J) and total DNA (DAPI) (K) from conditions in (I), $n = 2$ independent experiments. Comparisons were done via ordinary one-way ANOVA followed by Šidák's multiple comparison test. Mean and SEM. *$P < 0.05$, **$P < 0.01$, ***$P < 0,001$, and ****$P < 0.0001$.

Downloaded from https://www.science.org at University of Michigan Ann Arbor on March 07, 2025

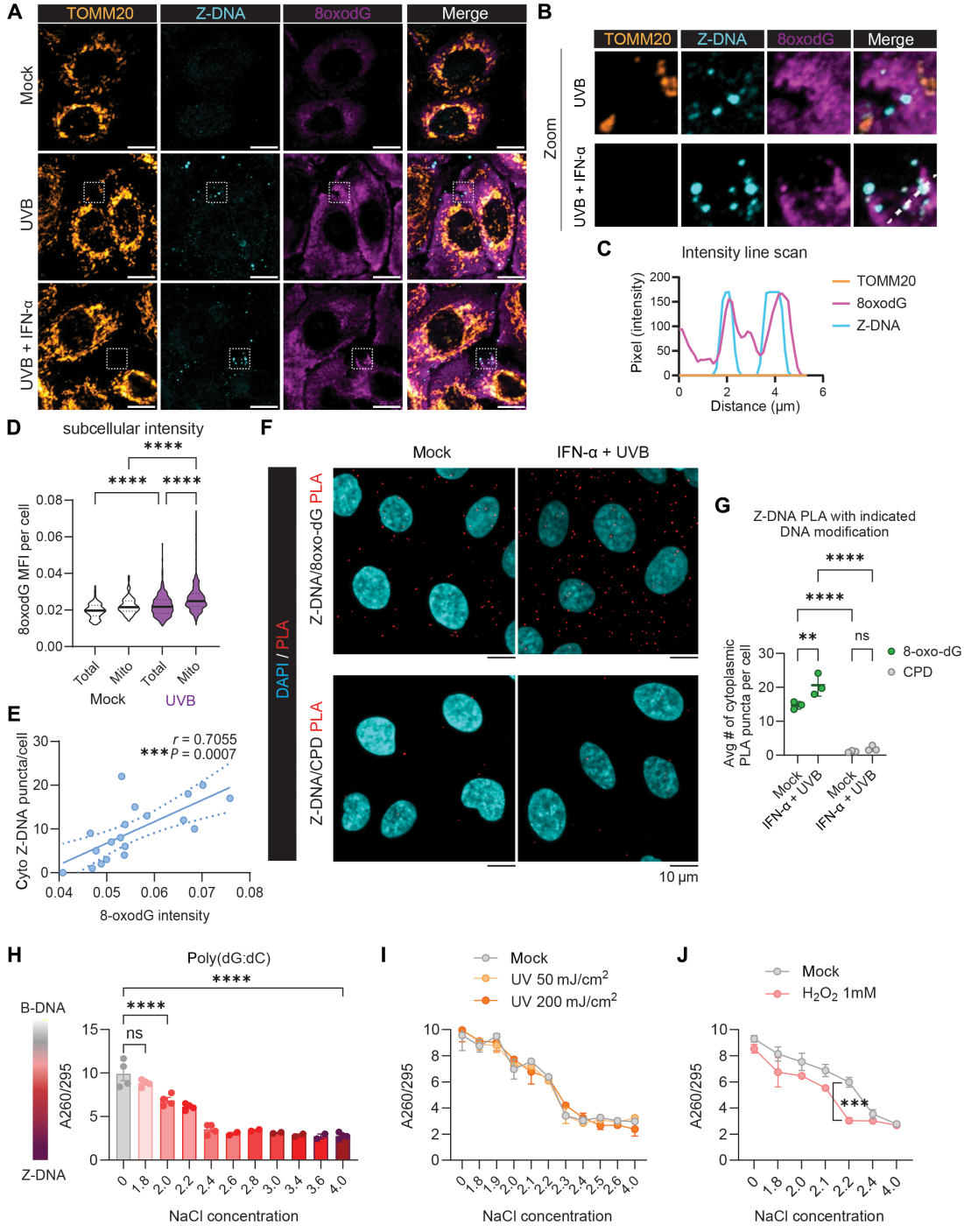


Fig. 3. UVB promotes Z-DNA formation via oxidative DNA damage. (**A**) Representative confocal images of the mitochondrial outer membrane (TOMM20), Z-DNA, and 8oxodG in N/TERTs at baseline, 3 hours after UVB exposure with or without IFN-α preincubation for 16 hours. Scale bars, 10 μm. (**B**) Magnified region from (A) highlighting proximity and colocalization of Z-DNA with intense 8oxodG staining in areas outside of mitochondria. (**C**) Representative line scan from Z-DNA puncta in (B) highlighting the absence of TOMM20 in spots of Z-DNA accumulation. (**D**) Subcellular intensity of mitochondrial versus total mean fluorescence intensity (MFI) of 8oxodG in UVB-treated N/TERTs 3 hours after UVB exposure ($n = 3$ independent experiments). (**E**) Correlation of the Z-DNA puncta per cell with matched average 8oxodG per cell. (**F**) Representative images of PLA of Z-DNA/8oxodG and Z-DNA/CPD in N/TERTs at baseline and 3 hours after UVB exposure. (**G**) Quantification of cytoplasmic PLA puncta per cell of Z-DNA/8oxodG and Z-DNA/CPD ($n = 3$). (**H**) Change of $A_{260/295}$ as a measure of B-DNA (high ratio ~ 10) versus Z-DNA (lower ratio of ~3) formation is graphed comparing low [NaCl] versus high [NaCl] conditions after 2 hours at 37°C. (**I**) Naked poly(dG:dC) was irradiated with the indicated UVB doses and incubated in the indicated [NaCl] as in (H) to induce Z-DNA. No shift to a lower ratio in lower [NaCl] was detected after UVB light exposure ($n = 3$). (**J**) To test the effect of oxidation on propensity for Z-DNA formation, poly(dG:dC) was treated with H_2O_2 (1 mM) for 2 hours at 37°C and subjected to varying NaCl concentrations as in (H) ($n = 3$). Buffers with indicated NaCl and H_2O_2 without DNA served as blanks for the assay. Comparisons were done via ordinary one-way or two-way ANOVA followed by Šidák's multiple comparison test. Mean and SEM. $^{**}P < 0.01$, $^{***}P < 0{,}001$, and $^{****}P < 0.0001$.

Downloaded from https://www.science.org at University of Michigan Ann Arbor on March 07, 2025

was independent of CLE subtype and the presence or absence of systemic disease (Fig. 4B). Furthermore, *ZBP1* expression correlated significantly with IFN scores in CLE, suggesting its up-regulation to be a phenomenon of cutaneous IFN expression rather than specific systemic clinical features (Fig. 4C). We confirmed these results in microarray datasets from patients with childhood SLE (cSLE; $n = 7$), where we observed significant up-regulation of *ZBP1* gene expression compared with that in CTLs ($n = 8$) and a significant correlation with the cutaneous IFN score (Fig. 4, D and E). To assess nonlesional *ZBP1* expression in the skin and identify which cells are expressing *ZBP1*, we used our single-cell sequencing dataset of patients with lupus ($n = 14$) compared with CTLs ($n = 14$) (*12*). We confirmed robust up-regulation of *ZBP1* in nonlesional and lesional KCs compared with those of CTLs (Fig. 4F). There was also a similar, but weaker, trend in cutaneous myeloid cells and endothelial cells; *ZBP1* expression was mostly undetectable in fibroblasts, melanocytes, and mast cells (Fig. 4F). We also looked at the expression of specific ZBP1 isoforms showing two long isoforms to be more abundantly expressed than the short isoform in nonlesional and lesional lupus skin compared with that of CTLs (fig. S4, A and B).

Further analysis of adult DM ($n = 41$) and juvenile DM (JDM) ($n = 9$) compared with CTLs ($n = 8$ and $n = 5$, respectively) revealed significant cutaneous *ZBP1* up-regulation in DM and JDM with significant correlation of *ZBP1* expression with the IFN score in adult DM (Fig. 4, G to I). In JDM, we were underpowered to observe a significant correlation between IFN score and *ZBP1*, but there was a similar trend (fig. S4C). The expression of *ZBP1* in lupus and DM skin samples did not correlate with autoantibody status, disease activity, or age (fig. S4, D and E), suggesting that the up-regulation of *ZBP1* is independent of these patient characteristics.

Next, we examined the protein expression of ZBP1 by staining skin samples from nonlesional and lesional lupus and DM skin. As expected, we observed increased ZBP1 in nonlesional and lesional discoid lupus erythematosus (DLE), subacute CLE (SCLE), and DM epidermis compared with CTL epidermis, where ZBP1 was basically undetectable (Fig. 4J). ZBP1 was highest expressed in the basal layer of the epidermis, whereas dermal staining was low. In summary, these results indicate that epidermal up-regulation of ZBP1 in nonlesional and lesional skin of autoimmune photosensitive diseases correlates with cutaneous IFN signatures and suggests that ZBP1 may be important for downstream immune responses in adult and pediatric CLE, SLE and DM skin.

Lupus KCs exhibit strong baseline and UV-induced cytosolic Z-DNA compared with CTL

Given enhanced IFN signaling and significant up-regulation of ZBP1 in lupus KCs, we quantified cytosolic Z-DNA puncta in primary control (CTL) and lupus KCs at baseline and after UVB exposure (Fig. 5A). At baseline, CTL KCs exhibited Z-DNA staining primarily within the mitochondrial network (Fig. 5A). After UVB exposure, we observed the enhanced total and cytosolic Z-DNA accumulation in CTL KCs (Fig. 5, A and B). Strikingly, lupus KCs exhibited enhanced total and cytosolic Z-DNA puncta at baseline that were significantly increased after UVB with formation of multiple large cytosolic puncta (Fig. 5, A and B). Preincubation of CTL KCs with IFN-α promoted enhanced cytosolic Z-DNA accumulation after UVB exposure, comparable to that in nonlesional lupus KCs after UVB alone, suggesting that the known chronic IFN loop in SLE KCs (*3*, *13*) stabilizes Z-DNA, potentially through the ISG *ZBP1*. Z-DNA accumulation in the cytosol after UVB exposure of lupus KCs was prevented by preincubation with mitoTEMPO, which led to the stabilization of Z-DNA within the mitochondrial network (Fig. 5C).

Given that UVB treatment of KCs up-regulates type I and type III IFNs, we examined whether mitoTEMPO also decreased UV-induced IFN gene expression in lupus primary KCs. In line with our microscopy data, we observed that mitoTEMPO led to significant down-regulation of *IFNB1*, *IFNL3*, and ISGs after UVB exposure (fig. S5, A and B). Baseline and UVB-induced cellular ROS were not increased in SLE KCs compared to primary CTL KCs (fig. S5C).

To further assess the role of ZBP1 in vivo, we assessed ZBP1 protein expression in lupus nonlesional skin samples collected by biopsy 24 hours after irradiation with a minimal erythema dose (MED) of UVB (Fig. 5D). Strikingly, in addition to the up-regulation of ZBP1 in nonlesional SLE skin compared with CTL skin, we observed enhanced expression and cytosolic localization of ZBP1 in the basal epidermis of nonlesional SLE skin after UV exposure (Fig. 5, E and F), suggesting a role for ZBP1 in UV-mediated responses in SLE in vivo. Together, these results show activation of the Z-DNA/ZBP1 pathway in SLE compared with CTL skin after UV exposure.

Z-DNA has stronger immunostimulatory properties than B-DNA to activate cGAS-STING–dependent IFN responses in human KCs

Z-DNA was recently described to bind ZBP1 and cGAS within the cytoplasm resulting in subsequent STING activation and sustained type 1 IFN responses (*34*). Hence, we next assessed the downstream effects of ZBP1 and DNA in the Z conformation on IFN activation in KCs.

First, we confirmed the up-regulation of *ZBP1* after IFN-α treatment in N/TERTs and primary KCs in vitro (fig. S6A). Next, we assessed colocalization of Z-DNA and ZBP1 after UVB with and without IFN-α priming. As shown in Fig. 6A, UV treatment induced some colocalization of large Z-DNA puncta and ZBP1 in the cytoplasm, whereas IFN-α priming followed by UVB resulted in strong colocalization even in small Z-DNA puncta (Fig. 6, A and B, and fig. S6B). These data are reflective of previous study results that found that ZBP1 and Z-DNA form a cytosolic complex and that type I IFNs enhance this through the up-regulation of ZBP1 and increased Z-DNA formation (*34*). Furthermore, we observed both cytoplasmic localization of cGAS and colocalization with cytosolic Z-DNA puncta in KCs after IFN-α treatment and UVB exposure (fig. S6C).

To test whether Z-DNA promotes cGAS-dependent IFN signaling, we synthesized topologically constrained circular 74–base pair (bp) Z-DNA and B-DNA constructs with the same base sequence as previously described (Fig. 6C) (*34*, *49*). We measured the ratio of $A_{260/295}$ in our constructs and saw significant decreases in Z-DNA compared with B-DNA, similar to NaCl-dependent transition using poly(dG:dC) (Fig. 6D). Next, we transfected N/TERTs with equal concentrations of B-DNA and Z-DNA (1 μg/ml) and measured IFN and ISG expression as well as protein levels of secreted chemokines. Strikingly, *IFNB1* and *ISG15* gene expression were significantly enhanced in N/TERTs treated with Z-DNA compared with B-DNA, which was completely dependent on cGAS (Fig. 6E and fig. S6D). ISGs were also significantly increased 24 hours after transfection with Z-DNA compared with B-DNA, and this was also completely dependent on cGAS (Fig. 6F and fig. S6E). To confirm this on a protein level, we measured both CCL5 and CXCL10 via enzyme-linked

Downloaded from https://www.science.org at University of Michigan Ann Arbor on March 07, 2025

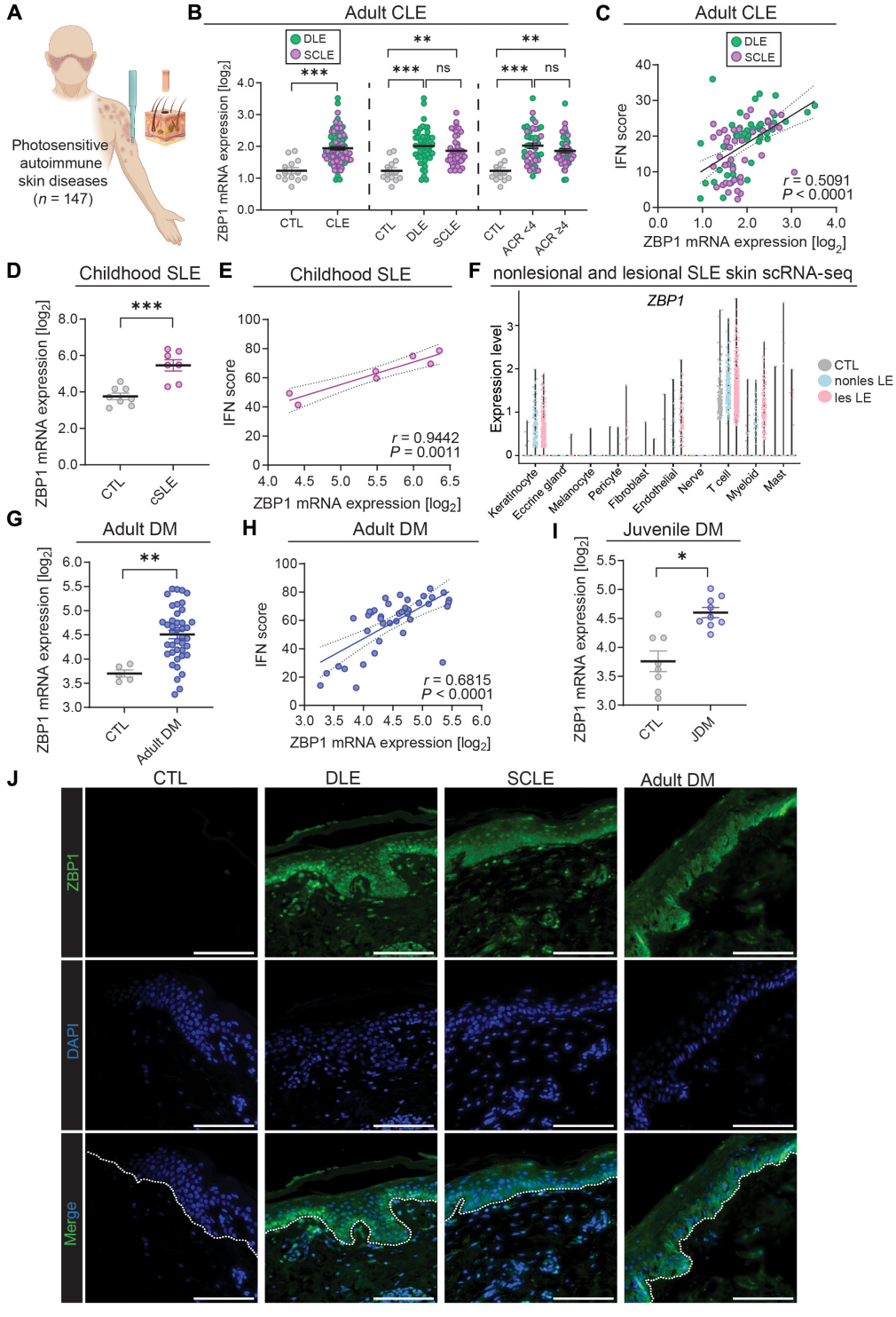


Fig. 4. Epidermal ZBP1 is overexpressed in autoimmune photosensitive diseases. (**A**) Graphical representation of data acquisition from lesional skin biopsies. (**B**) *ZBP1* expression in lesional CLE ($n = 90$) compared with that in CTLs ($n = 13$) (left) by lesion subtype [DLE or SCLE (middle)] and based on the presence or absence of systemic lupus via >4 1997 ACR criteria (right). (**C**) Correlation of *ZBP1* expression in CLE with IFN score by linear regression. (**D**) *ZBP1* expression in cSLE ($n = 7$) compared with that in CTLs ($n = 8$). (**E**) Correlation of ZBP1 expression with IFN score in cSLE. (**F**) Violin plots showing *ZBP1* expression from single-cell RNA sequencing across cutaneous cell types from nonlesional lupus skin (NLE, $n = 14$) to lesional lupus skin (LLE, $n = 14$) compared with CTL skin ($n = 14$). (**G**) Expression of *ZBP1* in adult DM ($n = 41$) and (**H**) correlation with IFN score by linear regression. (**I**) *ZBP1* expression in JDM ($n = 9$) compared with that in CTLs ($n = 8$). (**J**) Representative images of tissue immunofluorescence of ZBP1 in CTLs ($n = 7$), DLE ($n = 8$), SCLE ($n = 5$), and DM ($n = 6$). Dotted white line indicates the dermo-epidermal junction. Scale bars, 100 μm. [(B), (D), (G), and (I)] Mean + SEM. *$q < 0.05$, **$q < 0.01$, and ***$q < 0.0001$ by significance analysis of microarrays (SAMs; see Materials and Methods). [(C), (E), and (H)] Pearson correlation analysis.

immunosorbent assay (ELISA). These chemokines were significantly higher in supernatants of N/TERTs after Z-DNA versus B-DNA transfection (Fig. 6G). Similarly, the secretion of these chemokines was completely dependent on cGAS (Fig. 6G). Next, we wanted to confirm whether STING was necessary for IFN up-regulation after transfection with Z-DNA constructs. STING was required for IFN and ISG gene expression (Fig. 6H and fig. S6F). Recently, it has been reported that lysosomal degradation of mtDNA limits type I IFN responses (*50*). Given that UV exposure is also associated with the activation of autophagy (*51*), we looked at the lysosomal marker lysosomal-associated membrane protein 1 (LAMP1) but found no colocalization with Z-DNA puncta (fig. S6D). Together, these data indicate

Downloaded from https://www.science.org at University of Michigan Ann Arbor on March 07, 2025

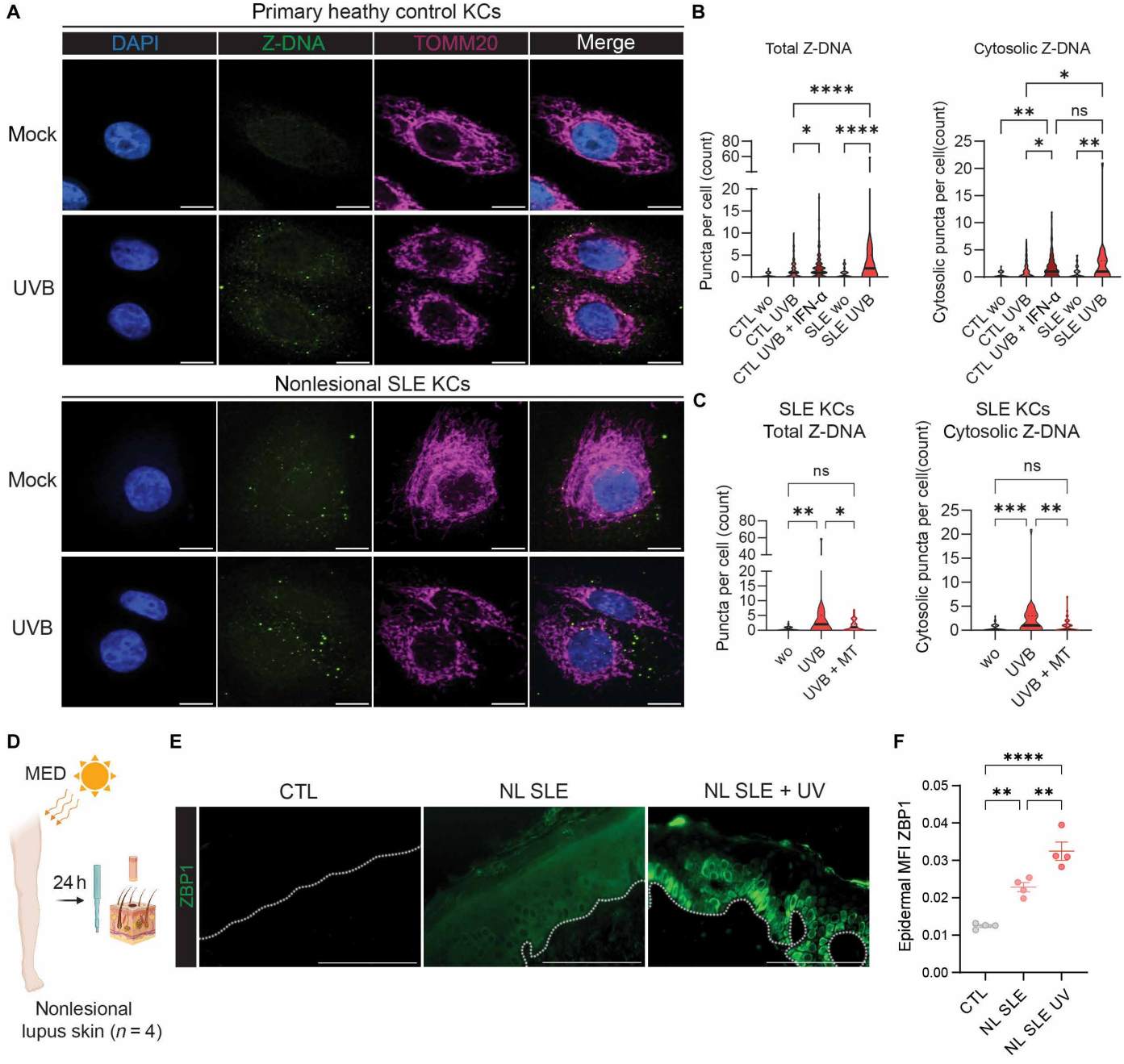


Fig. 5. Nonlesional lupus KCs exhibit cytosolic Z-DNA accumulation at baseline and after UVB exposure that is prevented by mitoTEMPO. (**A**) Representative images of confocal microscopy staining for Z-DNA, TOMM20, and counterstaining with DAPI at baseline and after UVB exposure and preconditioning with IFN-α (1000 U/ml for 16 hours before UVB exposure) in primary CTL KCs ($n = 4$) and SLE KCs ($n = 3$). (**B** and **C**) Quantification of total and cytosolic Z-DNA puncta after UVB with or without preincubation with mitoTEMPO or IFN-α using CellProfiler. (**D**) CTLs and patients with SLE ± UVB ($n = 4$ each group) were biopsied 24 hours after UV exposure with MED. (**E**) Representative images of ZBP1 staining in CTL, nonlesional SLE skin (NL SLE), and NL SLE after UV ($n = 4$ each group). Dotted white line indicates the dermo-epidermal junction. Scale bars, 100 μm. (**F**) Quantification of MFI of epidermal ZBP1 using open source CellProfiler software. Ordinary one-way ANOVA followed by Šidák's multiple comparison test. Mean and SEM. *$P < 0.05$, **$P < 0.01$, ***$P < 0.001$, and ****$P < 0.0001$.

that even late chemokine secretion after Z-DNA transfection is dependent on early cGAS-STING activation.

To identify in vivo evidence for activation of the STING pathway, we stained skin samples from CTLs and nonlesional SLE for pSTING before and 24 hours after UV exposure (Fig. 6I). Strikingly, nonlesional SLE skin exhibited pSTING expression in the basal epidermal layer without treatment, suggestive of chronic STING activation as a potential driver of IFN responses known to be elevated in SLE nonlesional skin. After UV light exposure, pSTING staining was evident in the basal epidermal layer in controls and was robustly

Downloaded from https://www.science.org at University of Michigan Ann Arbor on March 07, 2025

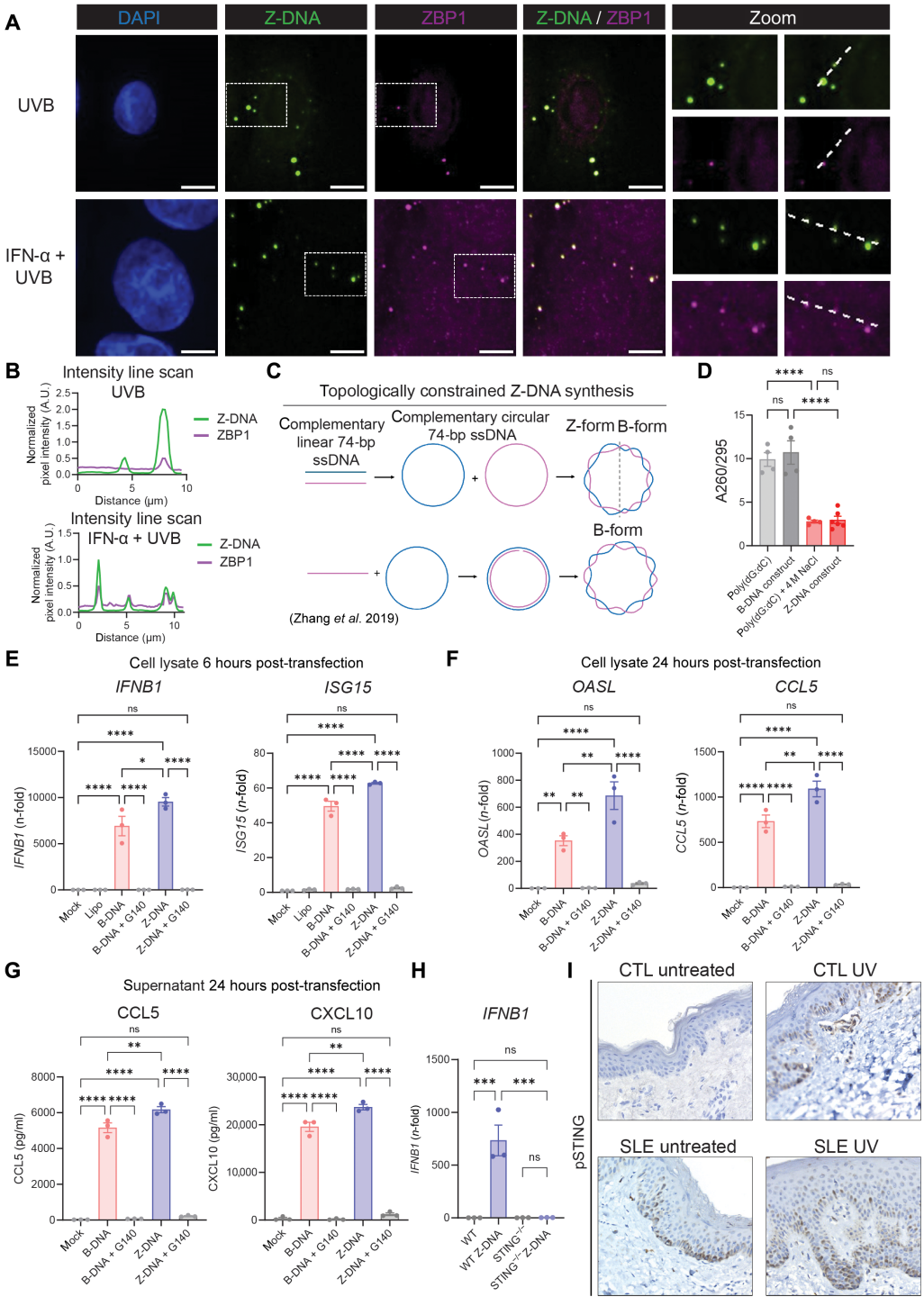


Fig. 6. Z-DNA binds to ZBP1, activates the cGAS-STING pathway, and has stronger immunostimulatory properties than B-DNA in KCs. (**A**) Representative images of confocal microscopy of N/TERTs after treatment with UVB ± IFN-α priming stained for Z-DNA, ZBP1, and DAPI. Dotted line indicates region chosen for intensity line scan analysis for (B). Scale bars, 5 μm. (**B**) Normalized intensity line scan of ZBP1 and Z-DNA after UVB and UVB + IFN-α priming (A.U., arbitrary unit). (**C**) Experimental approach for topologically constrained Z-DNA synthesis adapted from Zhang *et al.* (*49*). (**D**) $A_{260/295}$ for B-DNA/Z-DNA constructs in comparison with poly(dG:dC) ± 4 M NaCl ($n = 4$ to 6). (**E**) Gene expression analysis at 6 hours of indicated genes normalized to *RPLP0* from N/TERTs treated with Lipofectamine 2000 alone or transfected with Z-DNA or B-DNA (1 μg/ml) ($n = 3$). (**F**) Gene expression analysis 24 hours after DNA transfection with B-DNA or Z-DNA for indicated genes normalized to *RPLP0* ($n = 3$). (**G**) ELISA analysis of secreted chemokines from N/TERTs transfected with B-DNA or Z-DNA ± G140 (5 μM; cGAS inhibitor) ($n = 3$). (**H**) *IFNB1* gene expression normalized to *RPLP0* in wild-type (WT) and STING$^{-/-}$ KCs that have been transfected with Z-DNA (500 ng/ml) ($n = 3$). (**I**) Representative images of immunohistochemistry for pSTING in the skin of CTLs and patients with SLE before (untreated) and after UV exposure (UV) ($n = 5$ for each). Ordinary one-way ANOVA followed by Šidák's multiple comparison test. Mean and SEM. *$P < 0.05$, **$P < 0.01$, ***$P < 0.001$, and ****$P < 0.0001$.

Downloaded from https://www.science.org at University of Michigan Ann Arbor on March 07, 2025

activated in SLE skin (Fig. 6I). Together, these results confirm interaction of Z-DNA with ZBP1 in human KCs and identify Z-DNA as more immunostimulatory compared with B-DNA in a cGAS-STING dependent fashion.

ZBP1 is required for IFN signaling after UVB exposure and its up-regulation recapitulates an autoimmune photosensitive phenotype in KCs

Given that ZBP1 is up-regulated by IFN-α and that Z-DNA accumulation is enhanced by IFN-α priming before UVB treatment of KCs, we next wanted to explore whether knockdown of ZBP1 affected UVB-induced type I IFN responses, especially in an IFN-rich environment. We thus generated a knockdown of *ZBP1* using short hairpin RNA (shRNA) in N/TERTs (Fig. 7A and fig. S7, A and B). After UV exposure, KCs deficient in ZBP1 showed less type I and III IFN activation compared with controls (Fig. 7B). Priming with IFN-α before UVB exposure led to significant up-regulation of *IFNB1* and *IFNL3* gene expression in shcontrol KCs, whereas this enhancement was absent in shZBP1 KCs (Fig. 7B). The robust up-regulation of the ISG *CCL5* after priming with IFN-α before UV was also markedly decreased in the absence of ZBP1 (Fig. 7C). These results suggest that ZBP1 is required for UV-driven IFN responses and is particularly crucial for the effects of type I IFN priming on cGAS/STING activation and IFN production.

ZBP1 is increased in the epidermis of adult and cSLE as well as in adult and JDM, with the long isoform being overexpressed in lupus skin (Fig. 4, B to I, and fig. S4, A and B). To mimic the phenotype observed in these autoimmune photosensitive diseases, we generated a green fluorescent protein (GFP)–ZBP1–FLAG–tagged KC cell line of the long isoform [ZBP1 overexpressing (OE)] in N/TERTs and compared it with an N/TERT line expressing GFP alone (Fig. 7D and fig. S7, C and D). ZBP1 was primarily expressed in the cytoplasm in the OE cell line (fig. S7E). Given that ZBP1 is involved in panoptosis (*35*, *52*), we tested whether the overexpression of ZBP1 drives inflammatory cell death after UV exposure. Consistent with data suggesting that IFN priming followed by UV induces a pure apoptotic phenotype in KCs (*53*), ZBP1 OE KCs did not show increased LDH release 3 hours after UV exposure (fig. S7F). We next tested for IFN gene expression in ZBP1 OE KCs. Strikingly, we observed significant baseline up-regulation of both type I and III IFNs as well as ISGs in GFP-ZBP1-FLAG KCs compared with GFP KCs (Fig. 7E). In addition, confocal microscopy revealed cytosolic localization of cGAS in ZBP1 OE KCs, consistent with its activation (Fig. 7, F and G). Treatment of ZBP1 OE KCs with cGAS inhibitor G140 over 3 days resulted in significant down-regulation of ISGs, indicating that cGAS is required for chronic IFN activation in ZBP1 OE KCs (Fig. 7H and fig. S7G).

Next, we wanted to explore whether overexpression of ZBP1 was sufficient to increase cytosolic Z-DNA at baseline and after UV exposure. Cytosolic Z-DNA was increased at baseline in the ZBP1 OE KCs compared with controls (Fig. 7, I and J). After UVB exposure, we observed massive cytosolic Z-DNA accumulation in ZBP1 OE KCs compared with controls (Fig. 7, I and J). Mitochondrial fragmentation did not differ between ZBP1 OE KCs compared to controls (fig. S7H). These data suggest that ZBP1 overexpression is sufficient to promote Z-DNA stabilization and its downstream IFN signaling but does not affect mitochondrial health per se.

Together, these results indicate that up-regulation of ZBP1 is sufficient to stabilize Z-DNA and promote STING activation. ZBP1 is required for pro-inflammatory effects of type I IFNs on UV-mediated STING activation. Up-regulation of ZBP1 recapitulates the phenotype observed in autoimmune photosensitivity and explains the propensity for inflammatory rather than immunosuppressive responses upon UV exposure in a high–type I IFN environment (Fig. 8).

DISCUSSION

Here, we describe a pathway contributing to photosensitive responses in autoimmune patients. In KCs, chronic IFN-α exposure results in up-regulation of ZBP1, which stabilizes UVB-induced immunostimulatory Z-DNA derived from oxidized mtDNA leading to cGAS-STING–dependent type I and type III IFN production. Z-DNA is more immunostimulatory than B-DNA and leads to robust chemokine secretion in KCs. Knockdown of ZBP1 abrogated IFN responses in KCs, and overexpression of ZBP1 resulted in spontaneous IFN activation and Z-DNA accumulation in the cytoplasm. Our data support a growing list of studies that implicate mtDNA sensing in a variety of autoimmune diseases, including SLE and DM; here, we add skin responses to the list of affected organs and provide evidence for a role of ZBP1 in this process (*26*–*29*, *31*, *32*).

The effects of mtDNA oxidation and their contributions to SLE are numerous. Our data show that oxidative DNA lesions after UV exposure promote Z-DNA conformation. In lupus, oxidized mtDNA promotes IFN signaling in neutrophil extracellular traps (*28*, *29*). Furthermore, oxidized mtDNA induces a lupus-like phenotype in mice, and mtDNA derived from mitochondria-containing red blood cells drives IFN signaling in lupus monocytes (*31*, *54*). Whether Z conformation contributes to these phenotypes will require additional study. Oxidation of genomic DNA confers resistance to degradation by TREX1 and potentiates immunostimulation (*23*). Intriguingly, studies of bacterial biofilms containing extracellular Z-DNA derived from torsional stress have shown them to be resistant to nucleases. Our results show that intracellular oxidized mitochondrial Z-DNA is targetable through DNase I, which poses the question of whether not only the conformation alone but also the origin of Z-DNA confers resistance to nucleases. Another possibility is that once Z-DNA is stabilized by ZBP1, it might be more resistant to degradation than mitochondrial B-DNA.

Further, oxidized DNA in the skin of patients with lupus colocalizes with the ISG *MX1* (*23*), but evidence that lupus skin shows higher amounts of oxidative DNA lesions is lacking. Our data do not support a role for type I IFN in promotion of ROS in KCs. Rather, our model suggests that oxidized DNA damage by UV results in Z-DNA conformation and that stabilization of the Z-DNA by the ISG *ZBP1* is critical to promote more inflammation in diseases such as SLE and DM.

Our data also prompt the question of whether oxidized mtDNA from other cell types, including immune cells, is likely to transition to Z-DNA and whether Z-DNA sensing may be a central mechanism of the disease-promoting IFN signaling in SLE. Up-regulation of ZBP1 is observed not only in lupus skin but also in peripheral blood of patients with SLE (*55*). Whether this up-regulation is functionally relevant and regulates responses to oxidized mtDNA in immune cells should be further investigated.

Autoantibodies against nucleic acids are a hallmark of SLE development (*56*). Patients with SLE exhibit autoantibodies against Z-DNA; this was described many years ago and confirmed recently (*57*, *58*). However, the substrates for generation of these antibodies

Downloaded from https://www.science.org at University of Michigan Ann Arbor on March 07, 2025

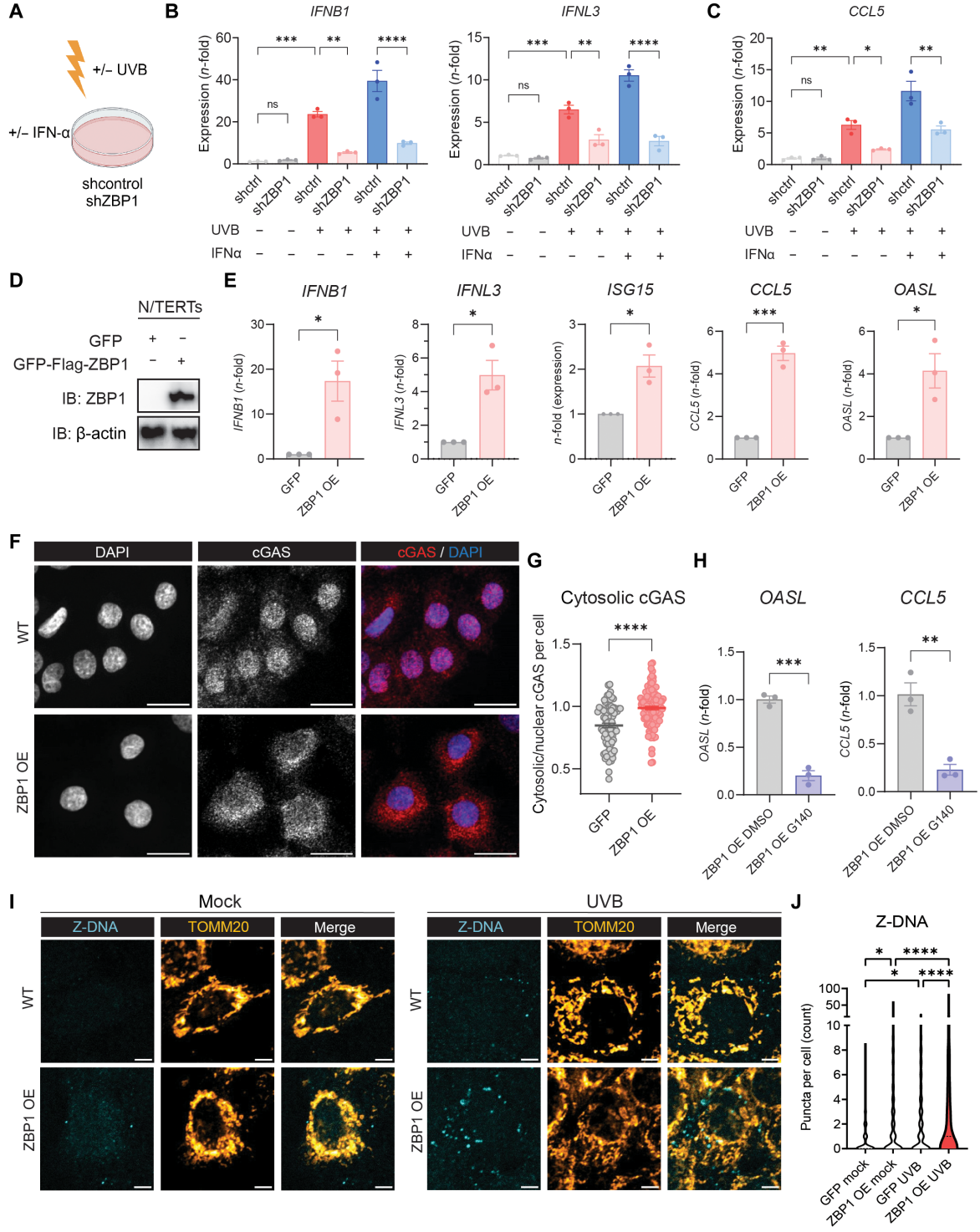


Fig. 7. ZBP1 regulates UVB-induced type I and III IFN responses in human keratinocytes. (**A** to **C**) Knockdown of ZBP1 in N/TERTs was performed using a lentivirus expressing either shRNA targeting human ZBP1 or shcontrol. Baseline, UV, and UV + IFN-α–induced gene expression were assessed for (B) type I and III IFNs (6 hours after UVB) and (C) CCL5, a known ISG (24 hours after UVB) ($n = 3$). (**D**) Generation of GFP/3XFLAG-tagged N/TERTs with overexpression of ZBP1 compared with GFP-tag only. (**E**) IFN genes and ISGs were assessed by real-time qtPCR at baseline in ZBP1 OE cells or GFP-expressing control N/TERTs (GFP) ($n = 3$). (**F**) Representative grayscale and merged images of confocal microscopy from N/TERTs with GFP or GFP-ZBP1 N/TERTs for cGAS (red) and DAPI (blue). Scale bars, 20 μm. (**G**) Quantification of cytosolic cGAS using ratio of cGAS MFI in the cytosol versus nuclear cGAS MFI using CellProfiler. (**H**) Gene expression analysis of ZBP1 OE KCs treated with cGAS inhibitor G140 (5 μM) for 3 days normalized to ZBP1 OE cells treated with DMSO ($n = 3$). (**I**) Representative confocal images of GFP-tagged N/TERTs or ZBP1-overexpressing N/TERTs of TOMM20 and Z-DNA at baseline and 3 hours after UVB exposure. Scale bars, 10 μm. (**J**) Quantification of cellular Z-DNA puncta in conditions from (I) using CellProfiler software. Ordinary one-way ANOVA followed by Šidák's multiple comparison test or *t* test. Mean and SEM. *$P < 0.05$, **$P < 0.01$, ***$P < 0.001$, and ****$P < 0.0001$.

Downloaded from https://www.science.org at University of Michigan Ann Arbor on March 07, 2025

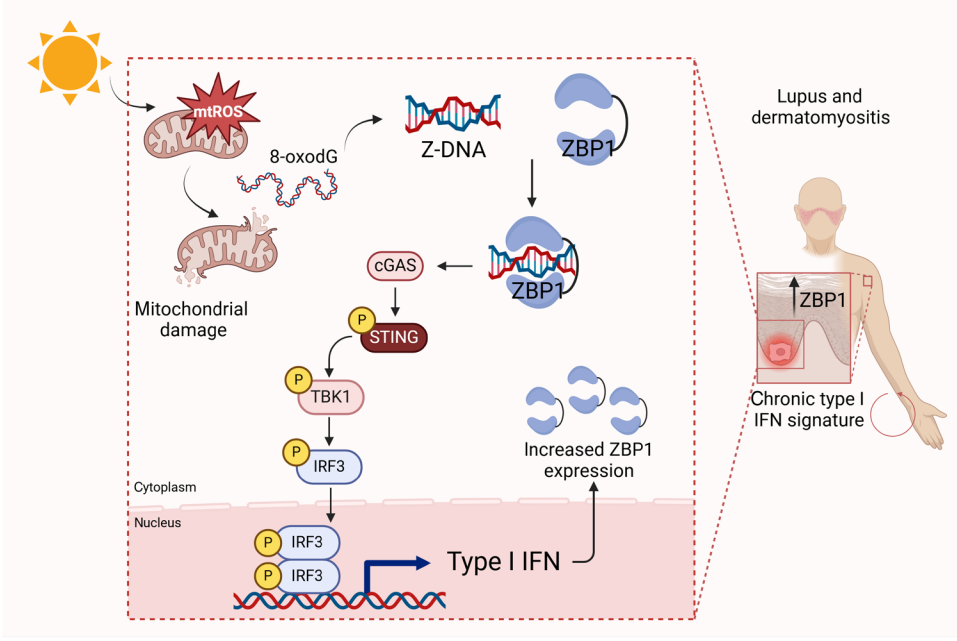


Fig. 8. Graphical summary. UV light promotes mtROS formation and mitochondrial damage, which results in the release of oxidized DNA that can promote Z-DNA conformation. In lupus and DM skin, Z-DNA is stabilized by ZBP1 and further activates the cGAS-STING–TANK binding kinase 1 (TBK1)–interferon regulatory factor 3 (IRF3) pathway to promote type I IFN secretion. This results in more ZBP1 expression, explaining the autocrine loop of type I IFN that is observed in photosensitive autoimmune diseases after UV light.

have not been studied. Given our data, it is intriguing to propose that Z-DNA derived from UV-irradiated KCs could also serve as an autoantigen and drive the adaptive immune response, especially in the context of UV-mediated systemic disease flares.

Epidermal type I IFN secretion including IFN-β and IFN-κ was shown to drive immune responses and enhanced cell death in the skin after UVB exposure (*11*). Other previous studies on mechanisms of photosensitivity in patients with lupus were performed in monogenic lupus, where cGAS-dependent IFN signaling has been described in TREX1 deficiency (*23*, *25*). Nuclear DNA fragments can be released during DNA repair processes, and the release of nuclear DNA due to rupture of the nuclear envelope can further activate cGAS-dependent IFN expression (*59*–*61*). This has been described in senescence and genetic instability syndromes such as Bloom syndrome (*59*, *61*–*63*). Whether nuclear DNA contributes to STING signaling in autoimmune photosensitivity seems unlikely based on our data and others'. First, the rate of skin cancer in autoimmune photosensitive diseases is not comparable to those with DNA repair deficiencies, indicating no persistence of increased nuclear DNA damage (*64*). Second, we did not see increase in UVB-mediated CPD formation with IFN-α priming, and there is evidence that type I IFN might even contribute to repair of CPDs (*65*). Third, mtDNA is more susceptible to oxidative modifications due to proximity to ROS production and insufficient DNA repair mechanisms compared with nuclear DNA (*19*, *22*, *66*). Fourth, we did not observe enhanced Z-DNA formation within the nucleus, any association of Z-DNA and CPDs via PLA, nor enhanced micronuclei after UV exposure, which can activate cGAS during genetic instability (*45*). Last, we showed that early type I IFN expression and mtDNA release upon UVB exposure was abrogated by the depletion of mtDNA.

We identified a critical role for ZBP1 in Z-DNA sensing and stabilization after UV exposure. ZBP1 is involved in multiple cellular processes in both antiviral defense via activation of the nuclear factor κB pathway and induction of PANoptosis (*36*, *37*, *67*–*70*). Furthermore, it can sustain IFN signaling after the release of mitochondrial Z-DNA after doxorubicin (*34*, *35*). So far, previous investigations used mostly murine data and investigated cell death pathways: Within the skin, murine ZBP1 was shown to drive necroptosis and autoinflammation only in receptor-interacting serine/threonine-protein kinase 1 (RIPK1)–deficient mice (*39*). In the presence of RIPK1, necroptotic signaling of ZBP1 is inhibited, and recent evidence revealed that ZBP1 interacts with RIPK1 to sustain IFN signaling in a STAT1-dependent manner (*34*, *39*). In our model, cells with overexpression of ZBP1 displayed a spontaneous type I IFN signature without a significant increase in cell death. This indicates that in an IFN-rich environment, as is seen in autoimmune photosensitive diseases, the primary role of ZBP1 is to bind ZDNA and regulate IFN signaling. It is possible that a second stimulus (such as inhibition of caspase-8 or down-regulation of RIPK1) is needed to confer cells toward an inflammatory cell death phenotype rather than innate immune activation. IFN-α priming alone promotes apoptotic death after UVB rather than activation of other cell death pathways (*53*). Thus, the IFN milieu could act as a "switch," which toggles the function of ZBP1 toward IFN secretion and apoptosis and away from panoptotic cell death. In contrast, diseases with increases in IFNγ show enhanced necroptosis of KCs. Thus, cell death phenotypes may depend on the inflammatory milieu and can be influenced by different IFN subtypes (*71*). ZBP1 can also activate the inflammasome via interaction with AIM2, apoptosis-associated speck-like protein containing a caspase recruitment domain (ASC), and pyrin to result in interleukin 1β secretion (*52*). Further evidence is needed to understand the role of ZBP1 in inflammasome and cell death pathways in the skin.

There are some limitations to our work reported here. First, we focused on early responses after UVB light exposure, but we did not assess cellular or transcriptional responses at later time points. Moreover, the direct interaction of ZBP1 with cGAS, AIM2, and other proteins through binding studies should be further investigated. In addition, other photosensitive disorders, such as porphyrias, which are driven by the accumulation of porphyrins due to deficiencies in

Downloaded from https://www.science.org at University of Michigan Ann Arbor on March 07, 2025

enzymes involved in hemoglobin metabolism (*72*), were not examined in this paper. How exactly tissue damage and photosensitivity occur in porphyria is currently not understood. Intriguingly, it was shown that ROS accumulate in porphyria, and, unexpectedly, certain porphyrins can stabilize Z-DNA (*73*). This raises the question of whether cutaneous Z-DNA might be involved in the entire spectrum of photosensitivity, not just those promoted by autoimmune diseases.

Together, our results uncover a mechanism of autoimmune photosensitivity driving innate immune responses in the skin of patients with lupus and DM that could be important for other photosensitive skin diseases. Both Z-DNA and ZBP1 represent previously unknown cutaneous targets for the prevention and potential treatment of lupus and DM skin disease.

MATERIALS AND METHODS

Study design

The aim of this study was to identify the drivers of an autocrine type I IFN loop after UV light exposure in autoimmune photosensitivity. KC cell lines and primary control and SLE KCs were used to examine mitochondrial dysfunction, Z-DNA formation, and cGAS/STING signaling in response to UV light through confocal microscopy and molecular biology techniques. Human skin biopsies from photosensitive diseases ($n = 147$ photosensitive patients and controls) were used to confirm in vivo relevance of Z-DNA/ZBP1/STING signaling downstream of UV light.

Human participants

All human participant protocols were reviewed and approved by the University of Michigan Institutional Review Board (IRB)–Med. The protocol number for human studies for KC cultures and single-cell RNA sequencing is HUM00151834, the IRB number for adult SLE and adult DM skin microarray data is HUM00072843, and the IRB for JDM and cSLE skin microarray data is HUM00231108. Skin samples from patients with SLE with a history of cutaneous lupus and sex- and age-matched healthy controls were obtained with written informed consent according to the Declaration of Helsinki.

Cell culture

Immortalized N/TERT KCs (N/TERT-2G) (*74*) were used with permission from J. G. Rheinwald (Brigham and Women's Hospital, Boston, MA, USA). N/TERTs were grown in KC serum-free medium (SFM) (Thermo Fisher Scientific, #17005-042) supplemented with bovine pituitary extract (30 μg/ml), epidermal growth factor (0.2 ng/ml), and 0.3 mM calcium chloride. N/TERTs were used from passage 6 to passage 20. Primary human KCs from patients with SLE and age- and sex-matched controls were isolated from nonlesional, non–sun-exposed skin as previously described (*13*) and used at passages 2 to 6 and grown in Epilife medium (Gibco, #MEPI500CA) with added human KC growth supplement (10 μl/ml medium). Demographics and clinical characteristics of patients and controls used for cell culture are shown in table S1. For IFN-α stimulation, we treated cells with an IFN-α final concentration of 1000 U/ml in KC SFM with added supplements.

Previously generated STING$^{-/-}$ KCs were used in this work and generated as previously described (*75*). N/TERTs overexpressing *ZBP1* were generated as follows: Full-length human ZBP1 cDNA, transcript variant 1, was obtained from GenScript (OHu21369). Polymerase chain reaction (PCR) was performed to add the 3XFlag tag to the N terminus of ZBP1 cDNA at the 5′ Not 1 site and 3′ Sal 1 site to facilitate cloning into expressing vector p3XFlag-CMV-7.1 (Sigma-Aldrich). The resulting plasmid containing the 3XFlag-ZBP1 was further subcloned in the Bst 1 and Bam HI sites of the vector pLVX-EF1α-AcGFP1-C1 (Takara, catalog no. 631984, simplified as pLvx-GFP) by PCR to generate the lentivirus OE vector pLVX-GFP-3XFlag-ZBP1 (simplified as pLvx-GFP-ZBP1OE). The constructs were confirmed by sequencing. For lentiviral infection, the lentiviral empty vector pLvx-GFP and OE pLvx-GFP-ZBP1OE were transiently transfected to 293T cells with packaging plasmids pxPAX2 and pMD2 using Lipofectamine 2000 to produce the lentivirus as described previously (*76*). The supernatant containing the lentivirus was used to infect the N/TERTs followed by puromycin selection at 10 μg/ml.

Knockdown of ZBP1 in N/TERTs was performed using a lentivirus expressing either shRNA targeting human ZBP1 or shcontrol. Two different mission lentivirus-based plasmids of shRNAs (clone numbers TRCN0000123050 and TRCN0000436778) against human ZBP1 and the shcontrol vector TRC2 pLKO.5-puro nonmammalian shRNA (SHC202) were obtained from Sigma-Aldrich (Burlington, MA). 293T cells were cotransfected with the shRNA and packaging plasmids psPAX2 and pMD2 using Lipofectamine 2000 (Invitrogen) in OptiMEM (Gibco) for 6 hours followed by replacing with KC medium to produce the lentivirus. Twenty-four hours after transfection, the virus-containing medium was collected and centrifuged for 5 min at 2000 rpm at 4°C. The resulting supernatant was supplemented with polybrene (8 μg/ml; Sigma-Aldrich) and used to infect the subconfluent N/TERTs. The 293T cells were replaced with fresh KC medium and were subsequently used to repeat the N/TERT cell infection two additional times at intervals of 8 to 12 hours. N/TERTs infected with either shRNA or shcontrol were selected at puromycin concentrations of 10 to 12 μg/ml, and cells were maintained in puromycin (10 μg/ml) until the day of the experiment.

UV irradiation

KCs were grown on either six-well plates on uncoated glass slides (22 mm by 22 mm; Thermo Fisher Scientific, #3406) for microscopy or 12-well plates for analysis of gene expression. On the day of UVB irradiation, medium was changed to prewarmed phosphate-buffered saline (PBS), and cells were irradiated with a dose of 50 mJ/cm^2 using the UV-2 ultraviolet irradiation system (Tyler Research). Emission of UVB radiation (310 nm) was allowed by cascade-phosphor ultraviolet generators. Immediately after irradiation, fresh prewarmed medium was added until further analysis.

mitoTEMPO treatment

To reduce mtROS, cells were incubated with mitoTEMPO (Sigma-Aldrich, SML0737) [50 μM in dimethyl sulfoxide (DMSO)] or 0.5% DMSO alone as a control 45 min before UVB exposure in KC SFM. After UVB exposure, fresh mitoTEMPO and medium were added to the wells until further analysis. No differences in MitoSOX staining, confocal microscopy, or gene expression were observed with phenol red–containing KC SFM versus phenol red–free medum; hence, phenol red–containing KC SFM was used. Rotenone was used as a positive control for mitoROS (0.5 μM).

Mitochondrial depolarization

For tracking mitochondrial depolarization, N/TERTs were seeded in a 96-well plate and irradiated in PBS (see the "UV irradiation"

Downloaded from https://www.science.org at University of Michigan Ann Arbor on March 07, 2025

section). Cells were stained immediately or at indicated times points 30 to 180 min after UVB. For mitochondrial polarization analysis, cells were incubated with MitoTracker Deep Red (50 ng/ml; Invitrogen, M22426), MitoTracker Green (50 ng/m; Invitrogen, M7514), and Hoechst 33342 (1 μg/ml) for 30 min at 37°C in KC SFM. Cells were washed 3× with medium and then immediately imaged, as described below.

Analysis of MitoSOX staining

KCs were first plated on glass-bottom (no. 1.5) 96-well MatTek dishes and grown for 36 hours. Cells were then pretreated with mitoTEMPO 45 min before UVB exposure and then irradiated in PBS (see mitoTEMPO treatment and UV irradiation) and incubated for 30 min. Within the last 20 min of the experiment, cells were stained with 2.5 μM MitoSOX red dye (Thermo Fisher Scientific, M36008) and Hoechst 33342 (1 μg/ml) for 20 min at 37°C, protected from light. Then, cells were washed with PBS and fixed with 4% paraformalaldehyde (PFA) at room temperature (RT) for 15 min. Last, cells were washed with PBS and then immediately imaged using a Nikon Yokogawa X1-CSU spinning disk confocal microscope. Fields of view were selected on the basis of the Hoechst stain.

Seahorse assay

The rate of oxygen consumption (OCR) of N/TERTs was measured using an Agilent Seahorse XF96 analyzer. N/TERTs were plated at 20,000 cells per well in a Seahorse 96-well assay plate and cultured overnight in KC SFM with added supplements. On the next day, the cells were washed and irradiated in PBS (see the "UV irradiation" section), and then PBS was replaced with Seahorse Dulbecco's modified Eagle's medium supplemented with the same levels of glucose, pyruvate, and glutamine without fetal bovine serum. Cells were kept in a 37°C incubator without CO_2 for 30 min before analysis. In all experiments, the Mito Stress Test Kit from Agilent was used to probe different aspects of mitochondrial function with respiratory chain inhibitors, 1.5 μM oligomycin, 2 μM carbonyl cyanide *p*-trifluoro-methoxyphenylhydrazone (FCCP), 0.5 μM rotenone, and 0.5 μM antimycin A. FCCP was titrated in a pilot experiment to determine optimal induction of maximal respiration. Because we have observed that cell density does not correlate linearly with extracellular flux measurements, we did not normalize OCR or extracellular acidification rate measurements. Basal respiration was normalized to mock condition.

RNA isolation, cDNA synthesis, and quantitative PCR

For RNA isolation, the Qiagen RNeasy Plus Mini kit was used according to the manufacturer's instructions. After isolation of RNA, samples were diluted in 20 to 40 μl of RNase-free water, depending on target RNA concentrations desired. Total RNA quantification and RNA purity were determined on the basis of the ratio $A_{260\,nm}/A_{280\,nm}$ using Thermo Fisher Scientific NANO drop 2000. A total of 500 to 1000 ng of cDNA was synthesized using the iScript cDNA synthesis kit (Bio-Rad, #1708891). cDNA (10 ng) was used for quantitative PCR in technical triplicates in a 384-well plate using SYBR Green Supermix (Applied Biosystems). PCR was run in Applied Biosystems QuantStudio 12 K Flex Real-Time PCR at the Advanced Genomics Core at the University of Michigan. Primer sequences are summarized in table S4. Gene expression level was determined by relating to the housekeeper gene β-actin or RPLP0 using the ΔΔCt method setting the mock condition to one.

Cellular fractionation

The isolation of cytosolic extracts was performed following Bryant *et al.* (*77*). Briefly, N/TERTs were trypsinized off an 80% confluent 10-cm plate, resuspended in 1 ml of ice-cold PBS, and divided into two portions (A and B). Sample A was treated with SDS to isolate the whole-cell lysate (WCL). Sample B was treated with digitonin lysis buffer [150 mM NaCl, 50 mM Hepes (pH 7.4), and digitonin (5 mg/ml)], incubated end over end for 10 min at 4°C and centrifuged at 950*g* for 5 min at 4°C to isolate the cytosolic fraction (supernatant). The pellets were washed and treated with 1% NP-40 [50 mM tris (pH 7.5), 0.15 M NaCl, 1 mM EDTA, 1% NP-40, and 10% glycerol] for 30 min and centrifuged at 17,000*g* at 4°C to isolate the mitochondrial fraction (supernatant). The nuclear fraction was obtained by treating the remaining pellet with SDS lysis buffer [20 mM tris (pH 8) and 1% SDS). The samples were boiled at 95°C for 5 min and centrifuged at 17,000*g* for 5 min at RT. All fractions were treated with RNase A (50 mg/ml) for 1.5 hours at 37°C and proteinase K (200 mg/ml) for 1 hour at 55°C before being subjected to phenol/chloroform-based DNA isolation. For quantifying cytosolic mtDNA abundance, DNA from each fraction was used for quantitative PCR (qtPCR) of mitochondrial gene abundance normalized to nuclear DNA in the WCL using primers for nuclear 18*S* ribosomal RNA (rRNA) (table S4). Total mtDNA was quantified using the WCL.

Depletion of mtDNA using ddC

To reduce total mtDNA content, we treated N/TERTs with ddC according to a previously published protocol (*77*) with the following modifications: N/TERTs were seeded in a six-well plate at 15 to 20% confluency and 12 hours after seeding medium was changed containing ddC (50 and 150 μM). Medium was changed every 24 hours until confluency reached 70 to 80% after 2 days. Then, cells were irradiated with UVB exposure (see above). Z-DNA staining was assessed 3 hours after UVB exposure, and gene expression was assessed 6 hours after irradiation. For mtDNA abundance after ddC treatment, N/TERTs were treated with SDS to isolate the WCL. The samples were boiled at 95°C for 5 min and centrifuged at 17,000*g* for 5 min at RT. Next, samples were treated with RNase A (50 mg/ml) for 1.5 hours at 37°C and proteinase K (200 mg/ml) for 1 hour at 55°C before being subjected to phenol/chloroform-based DNA isolation. Mitochondrial DNA abundance was determined by qtPCR using primers for mitochondrial genes (table S4) normalized to *18S*.

Cellular ROS measurement

For detection of cellular ROS, we used the indicator CM-H_2DCFDA (Invitrogen), and cells were incubated with CM-H_2DCFDA 10 μM for 30 min before UVB exposure. Phenol red–free KC medium (Gibco) was added, and fluorescence was measured 5 min after UVB exposure using a microplate reader (excitation/emission, 492/527 nm). The average of three to five replicates per condition was averaged in each experiment ($n = 4$ to 6), background fluorescence was subtracted, and data were expressed as fold change relative to untreated.

DNA transfection

N/TERTs were seeded in triplicates in a 24-well plate and grown for 48 hours in KC SFM to 70 to 80% confluence. DNA transfection was performed at RT using Lipofectamine 2000 and diluted circular double-stranded B-DNA and Z-DNA constructs. Lipofectamine 2000 (11668-029) and DNA were diluted in OptiMEM (Gibco, #31985-070) at a DNA ratio of 3 μl/μg. Cells were covered with

Downloaded from https://www.science.org at University of Michigan Ann Arbor on March 07, 2025

200 μl of OptiMEM containing 100 ng of DNA (1 μg DNA/ml of medium) or 50 ng of DNA (500 ng/ml) and incubated at 37°C until further analysis. Six and 24 hours after transfection, supernatants were saved, and cells were lysed in RLT plus buffer for gene expression using the QIAGEN RNeasy Plus Mini Kit and qtPCR (see above).

Immunofluorescence staining cell culture

KCs were plated on coverslips in a six-well plate. Mitochondrial ROS were stained 30 min after UVB exposure. 8oxodG, Z-DNA, and mitochondrial dynamics were stained 3 hours after UVB exposure. At each experimental end point, cells were fixed with freshly prepared 4% PFA at RT for 15 min. The immunofluorescence assay (IFA) was always performed on the same day as the experiment. After fixation, cells were washed and permeabilized with PBS + 0.1% Triton X-100 (wash buffer). When required, slides were treated with RNase A (1 mg/ml) or DNase I (200 U/ml) for 1 hour at 37°C. Then, cells were blocked with 5% bovine serum albumin (BSA) and 10% normal goat serum in wash buffer (block buffer) for 30 min at RT. Primary antibody cocktails were prepared in block buffer and incubated on each coverslip for 1 hour at RT. Then, wells were washed three times using wash buffer and incubated with secondary antibodies and counterstains diluted in block buffer for 30 min at RT. After this, wells were washed three times using wash buffer, and coverslips were mounted on glass slides using ProLong Glass Antifade Mountant (Invitrogen, P36980). Large (3 × 3) images were taken the next day either with ×60 or ×100 magnification, depending on the staining, on a Nikon Yokogawa spinning disk microscope. Using large image acquisition, more than 250 to 500 cells per condition could be stained. Specific antibody details are available in table S3. Operator bias was reduced during image acquisition through selection of fields of view and focal planes based on counterstains that were unrelated to the experimental question (DAPI or CellTracker).

Intensity line measurement

Representative images for intensity measurement were taken on a Nikon Yokogawa spinning disk microscope, and pixel intensity was assessed with Fiji (ImageJ) to measure indicated staining (TOMM20/Z-DNA/8oxodG or Z-DNA/ZBP1) intensity across the dotted lines at baseline and after UVB exposure ±IFN-α priming.

Automatic image analysis

Confocal microscopy images were quantified by automated image analysis using CellProfiler, an open-source software. All CellProfiler pipelines associated with this work are available in supplemental files (data file S1). Analysis of images was performed on raw images unless otherwise specified. Briefly, single cells were identified by nuclear objects on the basis of global thresholding of nuclear staining (DAPI or Hoechst) using the "identify primary objects" module, followed by propagation of the nuclear objects to the cellular periphery based on a whole-cell stain (CellTracker) using the identify secondary objects module. Subsequently, a variety of cellular parameters were measured and related to parent cells using the relate objects module. For the quantification of mitochondrial superoxide, the intensity of the mitochondrial superoxide indicator MitoSOX was analyzed within cells using Hoechst as the nuclear counterstain and defining cells by propagation of the nuclear objects to the cellular periphery on the basis of MitoSOX staining.

Mitochondria were determined using the TOMM20 immunostaining with two-class Otsu adaptive thresholding within the identify primary objects module, and the mitochondrial compartment was determined by using the "merge objects" to connect adjacent mitochondrial objects (neighbor distance of 0 pixels). To measure Z-DNA puncta outside of the mitochondrial compartment, puncta in the Z-DNA immunostaining were identified using the primary objects module. The cytosolic mitochondria-free content was created using the "identify tertiary objects" module by defining the nonnuclear compartment as the CellTracker-positive and DAPI-negative space and subsequently the cytosol by subtracting the mitochondrial staining (by TOMM20) from the nonnuclear compartment to get the mitochondria-free cytosolic compartment. Tertiary objects were then related to cells by using the "relate objects" module to determine cytosolic Z-DNA puncta per cell.

For analysis of 8oxodG, the intensity of the 8oxodG staining was analyzed within cell objects (defined as "total" in the manuscript) and within the mitochondrial compartment, which was defined by segmentation of mitochondrial staining (anti-TOMM20). For the correlation of 8oxodG with total and cytosolic Z-DNA, intensity values of 8oxodG per cell and Z-DNA puncta per cell across all images and different conditions were matched, and the average intensity of 8oxodG for the counts of Z-DNA puncta was calculated. The corresponding intensity to Z-DNA puncta counts was then plotted and correlated using Pearson correlation analysis. For correlation of mitochondrial fragments with total and cytosolic Z-DNA, mitochondrial fragments per cell were calculated, plotted against Z-DNA puncta counts per cell, and then correlated using Pearson correlation analysis.

Intensity values for DAPI were determined using nuclear intensity measurement in ImageJ. Intensity values for epidermal ZBP1 were determined using manual identification of the epidermis based on nuclear staining of slides with DAPI. Average intensity per image with similar epidermal areas including >300 cells were included in the analysis. cGAS intensity per cell was quantified within nuclear objects and the total cytoplasm (nuclear-subtracted cellular area based on GFP). The nuclear/cytoplasmic ratio was calculated by dividing nuclear and cytoplasmic intensity for each cell. Micronuclei were assessed using DAPI-stained images after UVB and IFN-α + UVB from three individual experiments. The frequency of micronuclei per 100 cells was counted manually. Micronuclei were not found in either condition.

The removal of outliers resulting from automated image analysis was performed using strict ROUT outlier identification ($Q = 0.1\%$) in GraphPad Prism from cell-level data pooled across multiple experiments. Operator bias during image acquisition was reduced by selecting fields of view and cells based on counterstains that were unrelated to the staining of primary interest.

Proximity ligation assay

N/TERTs were seeded in a 96-well plate (PhenoPlate, black, optically clear flat-bottom, cat. no.: 6055302, Revity) and grown until 80% confluency. Cells were treated ±IFN-α for 16 hours (1000 U/ml) ± UVB (50 mJ/cm^2) in PBS. For PLA, the Duolink PLA kit (DUO82049) was used. Three hours after irradiation, cells were fixed according to the manufacturer's instructions, and PLA was performed using Duolink In Situ PLA Probe Anti-Rabbit PLUS (DUO92002) and Duolink In Situ PLA Probe Anti-mouse MINUS (DUO92004) with Duolink In Situ Detection Reagents Red (DUO92008) for the following antibody

Downloaded from https://www.science.org at University of Michigan Ann Arbor on March 07, 2025

combinations: anti–Z-DNA (rabbit, 1:500) and anti-8oxodG (mouse, 1:500); Z-DNA (rabbit, 1:500) and anti-CPD (mouse, 1:500), anti–Z-DNA (rabbit, 1:500), and anti-DNA (mouse, 1:500); and anti-TOMM20 (rabbit, 1:500) and anti-PDH (mouse, 1:500). Isotype alone and secondary antibody only were used at dilutions matching the higher concentration of the primary anti-CPD antibody as negative controls. Images were taken using a Cell Voyager 8000 (CV8000, Yokogawa) as outlined below. Automatic image analysis of PLA was performed with CellProfiler software.

High-content confocal microscopy

For mitochondrial polarization and PLA analysis, cells were plated in 96-well imaging-grade microplates (PhenoPlate, Revvity, 6055302). Imaging was performed at 60×/1.2 numerical aperture magnification using a Cell Voyager 8000 (CV8000, Yokogawa) automated dual microlens spinning disk confocal microscope with water immersion. For mitochondrial polarization studies, live cells were imaged at 37°C in 5% CO_2. Maximum intensity projection images were collected across eight *z* planes spanning 8 μm. Eight to 12 fields of view were randomly selected within each well.

Measurement of B-DNA and Z-DNA conformation using a ratio of $A_{260/295}$

Conformation of Z-DNA and B-DNA was assessed using the absorbance ratio of 260 to 295 nm as previously described (*46*, *48*). We used poly(dG:dC) (50 ng/μl) for conformation analysis. Poly(dG:dC) was diluted in water with increasing salt concentrations (titration of 1.8, 2, 2.2, 2.4, 2.6, 2.8, 3, 3.2, 3.4, 3.6, and 4 M NaCl) to induce Z-DNA conformation. Reaction was performed for 2 hours at 37°C in nuclease-free microcentrifuge tubes (Bio-Rad). $A_{260/295}$ was measured with a NanoDrop (Thermo Fisher Scientific) using water with different salt concentrations as a blank. For induction of Z-DNA by H_2O_2, poly(dG:dC) was diluted in water containing 1 mM H_2O_2 and increasing salt concentrations as mentioned above. Samples were incubated for 2 hours at 37°C and were measured with a NanoDrop using 1 mM H_2O_2 with different salt concentrations (absent DNA) as blanks. Each incubation was performed in triplicates. The values were then plotted as the ratio of $A_{260/295}$.

Skin genome-wide expression datasets

Three previously published microarray datasets were used for analysis. These included samples from: (i) CTLs ($n = 13$) and lesional skin of patients with lupus ($n = 90$, of these 47 DLE and 43 SCLE) (*78*); (ii) CTLs ($n = 5$) and patients with DM ($n = 41$ biopsies from 36 patients) (*16*); and (iii) pediatric CTLs ($n = 8$) and patients with cSLE ($n = 7$ lesional skin biopsies from five patients) and JDM ($n = 9$ lesional skin biopsies from nine patients) (*79*). Microarray datasets are available from CLE through Gene Expression Omnibus (GEO) GSE81071, from adult DM through GSE142807, and from cSLE and JDM through GEO GSE148810. False discovery rate and log-fold change were calculated using a method from Tusher *et al.* (*80*) with unpaired two-class and 100 permutations in the significance analysis of microarrays module implemented in multiple experiment viewer (MeV), from the Institute for Genomic Research software suite. As we previously published, Pearson correlation analysis was performed between gene expression and a previously described 6 ISG score (*79*, *81*) using GraphPad Prism version 9.1.0.

Isoform expression of ZBP1

For both the keratinocytes and skin RNA sequencing data, we used SALMON (*82*). To quantify the isoform expression, with Genome Reference Consortium Human Build 38 (GRCh38) as genome reference, we used tximport to import the transcript abundance to R and used DESeq2 for modeling the count data and normalization (*50*). The estimated abundances for the three isoforms of *ZBP1* (i.e., ENST00000395822,ENST00000371173.8,andENST00000541799.1) were compared across different conditions.

Single-cell sequencing

For Fig. 4, the expression of *ZBP1* was examined from our single-cell RNA sequencing dataset in nonlesional ($n = 7$), lesional ($n = 7$), and CTL ($n = 14$) skin (*12*). Specifically, ZBP1 expression was plotted across the major cell types defined in the single-cell RNA sequencing dataset, and these cell types were further divided by the disease states of the cells.

Tissue immunofluorescence

To assess tissue protein expression, formalin-fixed, paraffin-embedded (FFPE) tissue slides were obtained from patients with CLE (chronic discoid lupus, SCLE, and nonlesional skin from patients with systemic lupus), DM (lesional and nonlesional skin), and CTLs. Slides were heated for 1 hour at 60°C and rehydrated, and antigen was retrieved with tris-EDTA (pH 6) in a pressure cooker water bath (125°C). After cooling, slides were blocked with blocking buffer (PBS + 10% normal goat serum) and then incubated with primary antibodies (diluted in blocking buffer) against ZBP1 (table S3) overnight at 4°C. Slides were incubated with secondary antibodies (table S3). Then, slides were mounted with Antifade glass mounting medium (Thermo Fisher Scientific) with DAPI and dried overnight at room temperature in the dark. Images were acquired using a Zeiss Axioskop 2 microscope and analyzed using CellProfiler (see above). Images presented are representative of at least five biological replicates. Patient characteristics for samples from patients with SCLE/DLE and DM are shown in table S2. Controls were anonymized biopsies from CTLs without history of skin disease.

Immunohistochemistry

For detection of pSTING (Ser^{366}) in the skin, FFPE sections were heated at 65°C for 30 min, deparaffinized, rehydrated, and heated at 100°C for 20 min in antigen retrieval buffer (pH 6). Slides were washed, treated with 3% hydrogen peroxide in PBS for 5 min, blocked (10% goat serum), and incubated with anti-pSTING (Ser^{366}) (1:100 dilution; Cell Signaling Technologies, E9A9KRabbit mAb #9359) overnight at 4°C. All slides were then incubated with for 30 min with goat anti-rabbit immunoglobulin G (H + L) biotinylated secondary antibody (1:200), followed by incubation with VECTASTAIN Elite ABC–horseradish peroxidase reagent R.T.U. (Vector Laboratories, SK-4105), followed by detection using 3,3′-diaminobenzidine tetrahydrochloride (DAB) substrate (Vector Laboratories) under a light microscope. Slides were then counterstained with hematoxylin, dehydrated, and mounted. Images were acquired using a Zeiss microscope (Zeiss, Oberkochen, Germany).

Topologically constrained Z-DNA synthesis

To synthesize circular Z-DNA and B-DNA, the protocol according to Zhang *et al.* (*49*) was used. First, 74-bp oligomers containing a 5′

Downloaded from https://www.science.org at University of Michigan Ann Arbor on March 07, 2025

phosphate modification (Sigma-Aldrich) were ligated to form circular single-stranded DNA (ssDNA) using the "step by step" approach in 0.1× T4 ligase buffer. The reaction mixture (total volume of 120 μl) contained 10 μM splint, T4 ligase (75 kU) (Thermo Fisher Scientific, EL0011), and 0.2× T4 ligase buffer (table S5). The corresponding substrate mix contained the 74-bp oligomer at 8 μM in 120 μl of 0.1× T4 ligase buffer (table S5). A total of 12 μl of the DNA mix was added to the reaction mix every 20 min at 25°C for a total of 12 additions, bringing the total reaction volume to 240 μl. After the final addition of DNA, the reaction continued for 12 hours at 25°C. The reaction was terminated by incubation at 65°C for 15 min. Remaining linear DNA substrate was degraded by addition of 28.6 μl 10× exonuclease I buffer and 20 μl of exonuclease I (Thermo Fisher Scientific, 720735KU) and incubation at 37°C for 2 hours followed by inactivation at 80°C for 20 min.

The formation of circular DNA was confirmed via gel electrophoresis using a 10% denaturing polyacrylamide gel containing 7 M urea (1× tris-borate EDTA buffer containing 89 mM tris-borate and 2 mM EDTA). DNA gel was then incubated with SYBR Green II for 10 min and imaged under UV light. Phenol/chloroform-based DNA extraction of the remaining substrate was performed, samples were dissolved and desalted by ethanol precipitation (100%, followed by 95 and 70%), and pellets were dissolved in 1 mM Hepes solution containing 1 mM $MgCl_2$ (pH 7.5). ssDNA strands were then annealed to form double-stranded B-DNA or Z-DNA as follows: Circular 74F ssDNA was annealed to circular 74R ssDNA strands at a 1:1 molar ratio in a thermocycler using the following steps: 90°C for 5 min, cool to 60°C via dropping by 0.1°C/s, hold at 60°C for 10 min, cool to 20°C at 0.1°C/s, and hold at 12°C. B-DNA was made by annealing linear 74F ssDNA to circular 74R ssDNA or annealing circular 74F ssDNA to linear 74R ssDNA as described above. After annealing, fully double-stranded B-DNA was obtained by incubating the dsDNA with T4 ligase in 1× T4 ligase buffer for 12 hours at 25°C, followed by incubation with exonuclease I for 2 hours at 37°C and enzyme inactivation at 80°C for 20 min. Both B-DNA and Z-DNA were then purified by phenol/chloroform extraction and ethanol precipitation. Purified DNA pellets were redissolved in 10 mM Hepes buffer [10 mM $MgCl_2$ (pH 7.5)] and used for further experiments. Confirmation of B-DNA and Z-DNA constructs was performed by obtaining the $A_{260/295}$ ratio for each synthesized sample before further use. For DNA transfection of synthesized constructs, B-DNA and Z-DNA were diluted to equal concentrations (100 ng/μl) in 10 mM Hepes buffer containing 10 mM $MgCl_2$ before the addition of OptiMEM and Lipofectamine (see the "DNA transfection" section).

Western blotting

Cells were washed with ice-cold PBS and then lysed. Before SDS–polyacrylamide gel electrophoresis (SDS-PAGE), sample protein content was normalized by dilution after a Bradford assay. Samples were diluted in Laemmli sample loading buffer supplemented with β-mercaptoethanol (Bio-Rad), heated for 5 min at 95°C, and then separated on 4 to 20% gradient polyacrylamide tris-glycine gels (Bio-Rad) or NuPAGE 4 to 12% bis-tris gel (Invitrogen). After SDS-PAGE, gels were transferred to a 0.45-μm nitrocellulose membrane or polyvinylidene difluoride membranes by Trans-Blot Turbo transfer system (Bio-Rad), and membranes were blocked with PBS + 5% BSA + 0.1% Tween 20 (blocking buffer) for 30 min at room temperature on a shaker. After blocking, primary antibodies were diluted in signal enhancer HIKAR solution 1 (Nacalai USA) and incubated overnight at 4°C on a shaker. Secondary antibodies diluted in signal enhancer HIKAR solution 2 (Nacalai USA) were added and incubated for 30 min at room temperature. Detection by enhanced chemiluminescence was carried out with a SuperSignal West Dura kit (Thermo Fisher Scientific, catalog no. 34075), followed by imaging on Omega Lum C (Aplegen). Antibodies and dilutions for Western blot are listed in table S3. Uncropped blots can be seen in data file S2.

Enzyme-linked immunosorbent assay

Twenty-four hours after DNA transfection with B-DNA/Z-DNA constructs, cell culture supernatants were collected and centrifuged at 2000*g* for 5 min at RT to remove cellular debris. CCL5 (DY278, R&D Systems) and CXCL10 (DY266, R&D Systems) were measured by ELISA by the University of Michigan Cancer Center Immunology Core.

Lactate dehydrogenase cytotoxicity assay

To measure cytotoxicity in ZBP1 OE KCs and GFP control KCs, N/TERTs were seeded in triplicates in a 96-well plate. Cells were treated with UVB (20 and 50 mJ/cm^2) in PBS. After irradiation, cells incubated in KC SFM + supplements for 4 hours. Cytotoxicity was assessed using the CyQUANT LDH Cytotoxicity Assay Kit (Invitrogen, C20300) according to the manufacturer's instructions.

Supplementary Materials

The PDF file includes:

Figs. S1 to S7
Tables S1 to S5

Other Supplementary Material for this manuscript includes the following:

Data files S1 to S3
MDAR Reproducibility Checklist

REFERENCES AND NOTES

1. J. Wenzel, Cutaneous lupus erythematosus: New insights into pathogenesis and therapeutic strategies. *Nat. Rev. Rheumatol.* **15**, 519–532 (2019).
2. S. N. Estadt, M. P. Maz, J. Musai, J. M. Kahlenberg, Mechanisms of photosensitivity in autoimmunity. *J. Invest. Dermatol.* **142**, 849–856 (2022).
3. M. K. Sarkar, G. A. Hile, L. C. Tsoi, X. Xing, J. Liu, Y. Liang, C. C. Berthier, W. R. Swindell, M. T. Patrick, S. Shao, P. S. Tsou, R. Uppala, M. A. Beamer, A. Srivastava, S. L. Bielas, P. W. Harms, S. Getsios, J. T. Elder, J. J. Voorhees, J. E. Gudjonsson, J. M. Kahlenberg, Photosensitivity and type I IFN responses in cutaneous lupus are driven by epidermal-derived interferon kappa. *Ann. Rheum. Dis.* **77**, 1653–1664 (2018).
4. J. H. Sim, W. G. Ambler, I. F. Sollohub, M. J. Howlader, T. M. Li, H. J. Lee, T. T. Lu, Immune cell–stromal circuitry in lupus photosensitivity. *J. Immunol.* **206**, 302–309 (2021).
5. K. Foering, A. Y. Chang, E. W. Piette, A. Cucchiara, J. Okawa, V. P. Werth, Characterization of clinical photosensitivity in cutaneous lupus erythematosus. *J. Am. Acad. Dermatol.* **69**, 205–213 (2013).
6. M. P. Maz, J. W. S. Martens, A. Hannoudi, A. L. Reddy, G. A. Hile, J. M. Kahlenberg, Recent advances in cutaneous lupus. *J. Autoimmun.* **132**, 102865 (2022).
7. S. Skopelja-Gardner, J. Tai, X. Sun, L. Tanaka, J. A. Kuchenbecker, J. M. Snyder, P. Kubes, T. Mustelin, K. B. Elkon, Acute skin exposure to ultraviolet light triggers neutrophil-mediated kidney inflammation. *Proc. Natl. Acad. Sci. U.S.A.* **118**, e2019097118 (2021).
8. K. L. Clark, T. J. Reed, S. J. Wolf, L. Lowe, J. B. Hodgin, J. M. Kahlenberg, Epidermal injury promotes nephritis flare in lupus-prone mice. *J. Autoimmun.* **65**, 38–48 (2015).
9. E. L. Gutmark, D. Q. Lin, I. Bernstein, S. Q. Wang, B. F. Chong, Sunscreen use in patients with cutaneous lupus erythematosus. *Br. J. Dermatol.* **173**, 831–834 (2015).
10. A. Psarras, A. Alase, A. Antanaviciute, I. M. Carr, M. Y. Md Yusof, M. Wittmann, P. Emery, G. C. Tsokos, E. M. Vital, Functionally impaired plasmacytoid dendritic cells and non-haematopoietic sources of type I interferon characterize human autoimmunity. *Nat. Commun.* **11**, 6149 (2020).
11. A. Psarras, M. Wittmann, E. M. Vital, Emerging concepts of type I interferons in SLE pathogenesis and therapy. *Nat. Rev. Rheumatol.* **18**, 575–590 (2022).

Downloaded from https://www.science.org at University of Michigan Ann Arbor on March 07, 2025

12. A. C. Billi, F. Ma, O. Plazyo, M. Gharaee-Kermani, R. Wasikowski, G. A. Hile, X. Xing, C. M. Yee, S. M. Rizvi, M. P. Maz, C. C. Berthier, F. Wen, L. C. Tsoi, M. Pellegrini, R. L. Modlin, J. E. Gudjonsson, J. M. Kahlenberg, Nonlesional lupus skin contributes to inflammatory education of myeloid cells and primes for cutaneous inflammation. *Sci. Transl. Med.* **14**, eabn2263 (2022).
13. J. N. Stannard, T. J. Reed, E. Myers, L. Lowe, M. K. Sarkar, X. Xing, J. E. Gudjonsson, J. M. Kahlenberg, Lupus skin is primed for IL-6 inflammatory responses through a keratinocyte-mediated autocrine type I interferon loop. *J. Invest. Dermatol.* **137**, 115–122 (2017).
14. L. C. Tsoi, G. A. Hile, C. C. Berthier, M. K. Sarkar, T. J. Reed, J. Liu, R. Uppala, M. Patrick, K. Raja, X. Xing, E. Xing, K. He, J. E. Gudjonsson, J. M. Kahlenberg, Hypersensitive IFN responses in lupus keratinocytes reveal key mechanistic determinants in cutaneous lupus. *J. Immunol.* **202**, 2121–2130 (2019).
15. M. M. Tabata, L. M. Hodgkinson, T. T. Wu, S. Li, C. Huard, S. Zhao, D. Bennett, J. Johnson, C. Tierney, W. He, J. E. Buhlmann, K. M. Page, K. Johnson, L. Casciola-Rosen, L. Chung, K. Y. Sarin, D. Fiorentino, The type I interferon signature reflects multiple phenotypic and activity measures in dermatomyositis. 75, 1842–1849 (2023).
16. L. C. Tsoi, M. Gharaee-Kermani, C. C. Berthier, T. Nault, G. A. Hile, S. N. Estadt, M. T. Patrick, R. Wasikowski, A. C. Billi, L. Lowe, T. J. Reed, J. E. Gudjonsson, J. M. Kahlenberg, IL18-containing 5-gene signature distinguishes histologically identical dermatomyositis and lupus erythematosus skin lesions. *JCI Insight* **5**, e139558 (2020).
17. R. R. Goel, S. V. Kotenko, M. J. Kaplan, Interferon lambda in inflammation and autoimmune rheumatic diseases. *Nat. Rev. Rheumatol.* **17**, 349–362 (2021).
18. S. Zahn, C. Rehkämper, B. M. Kümmerer, S. Ferring-Schmidt, T. Bieber, T. Tüting, J. Wenzel, Evidence for a pathophysiological role of keratinocyte-derived type iii interferon (IFNλ) in cutaneous lupus erythematosus. *J. Invest. Dermatol.* **131**, 133–140 (2011).
19. M. A. Birch-Machin, E. V. Russell, J. A. Latimer, Mitochondrial DNA damage as a biomarker for ultraviolet radiation exposure and oxidative stress. *Br. J. Dermatol.* **169**, 9–14 (2013).
20. R. Jugé, J. Breugnot, C. Da Silva, S. Bordes, B. Closs, A. Aouacheria, Quantification and characterization of UVB-induced mitochondrial fragmentation in normal primary human keratinocytes. *Sci. Rep.* **6**, 35065 (2016).
21. C. Li, Y. Zhu, W. Liu, W. Xiang, S. He, T. Hayashi, K. Mizuno, S. Hattori, H. Fujisaki, T. Ikejima, Impaired mitophagy causes mitochondrial DNA leakage and STING activation in ultraviolet B-irradiated human keratinocytes HaCaT. *Arch. Biochem. Biophys.* **737**, 109553 (2023).
22. I. Golovynska, S. Golovynskyi, J. Qu, Comparing the impact of NIR, visible and UV Light on ROS upregulation via photoacceptors of mitochondrial complexes in normal, immune and cancer cells. *Photochem. Photobiol.* **99**, 106–119 (2023).
23. N. Gehrke, C. Mertens, T. Zillinger, J. Wenzel, T. Bald, S. Zahn, T. Tüting, G. Hartmann, W. Barchet, Oxidative damage of DNA confers resistance to cytosolic nuclease TREX1 degradation and potentiates STING-dependent immune sensing. *Immunity* **39**, 482–495 (2013).
24. S. Skopelja-Gardner, J. An, J. Tai, L. Tanaka, X. Sun, P. Hermanson, R. Baum, M. Kawasumi, R. Green, M. Gale Jr., A. Kalus, V. P. Werth, K. B. Elkon, The early local and systemic type I interferon responses to ultraviolet B light exposure are cGAS dependent. *Sci. Rep.* **10**, 7908 (2020).
25. N. Berndt, C. Wolf, K. Fischer, E. Cura Costa, P. Knuschke, N. Zimmermann, F. Schmidt, M. Merkel, O. Chara, M. A. Lee-Kirsch, C. Günther, Photosensitivity and cGAS-dependent IFN-1 activation in patients with lupus and TREX1 deficiency. *J. Invest. Dermatol.* **142**, 633–640.e6 (2022).
26. J. S. Riley, S. W. Tait, Mitochondrial DNA in inflammation and immunity. *EMBO Rep.* **21**, e49799 (2020).
27. A. P. West, G. S. Shadel, Mitochondrial DNA in innate immune responses and inflammatory pathology. *Nat. Rev. Immunol.* **17**, 363–375 (2017).
28. C. Lood, L. P. Blanco, M. M. Purmalek, C. Carmona-Rivera, S. S. De Ravin, C. K. Smith, H. L. Malech, J. A. Ledbetter, K. B. Elkon, M. J. Kaplan, Neutrophil extracellular traps enriched in oxidized mitochondrial DNA are interferogenic and contribute to lupus-like disease. *Nat. Med.* **22**, 146–153 (2016).
29. S. Caielli, S. Athale, B. Domic, E. Murat, M. Chandra, R. Banchereau, J. Baisch, K. Phelps, S. Clayton, M. Gong, T. Wright, M. Punaro, K. Palucka, C. Guiducci, J. Banchereau, V. Pascual, Oxidized mitochondrial nucleoids released by neutrophils drive type I interferon production in human lupus. *J. Exp. Med.* **213**, 697–713 (2016).
30. N. Miao, Z. Wang, Q. Wang, H. Xie, N. Yang, Y. Wang, J. Wang, H. Kang, W. Bai, Y. Wang, R. He, K. Yan, Y. Wang, Q. Hu, Z. Liu, F. Li, F. Wang, F. Ginhoux, X. Zhang, J. Yin, L. Lu, J. Wang, Oxidized mitochondrial DNA induces gasdermin D oligomerization in systemic lupus erythematosus. *Nat. Commun.* **14**, 872 (2023).
31. S. Caielli, J. Cardenas, A. A. de Jesus, J. Baisch, L. Walters, J. P. Blanck, P. Balasubramanian, C. Stagnar, M. Ohouo, S. Hong, L. Nassi, K. Stewart, J. Fuller, J. Gu, J. F. Banchereau, T. Wright, R. Goldbach-Mansky, V. Pascual, Erythroid mitochondrial retention triggers myeloid-dependent type I interferon in human SLE. *Cell* **184**, 4464–4479.e19 (2021).
32. L. E. Newman, G. S. Shadel, Mitochondrial DNA release in innate immune signaling. *Annu. Rev. Biochem.* **92**, 299–332 (2023).
33. A. P. West, W. Khoury-Hanold, M. Staron, M. C. Tal, C. M. Pineda, S. M. Lang, M. Bestwick, B. A. Duguay, N. Raimundo, D. A. MacDuff, S. M. Kaech, J. R. Smiley, R. E. Means, A. Iwasaki, G. S. Shadel, Mitochondrial DNA stress primes the antiviral innate immune response. *Nature* **520**, 553–557 (2015).
34. Y. Lei, J. J. VanPortfliet, Y. F. Chen, J. D. Bryant, Y. Li, D. Fails, S. Torres-Odio, K. B. Ragan, J. Deng, A. Mohan, B. Wang, O. N. Brahms, S. D. Yates, M. Spencer, C. W. Tong, M. W. Bosenberg, L. C. West, G. S. Shadel, T. E. Shutt, J. W. Upton, P. Li, A. P. West, Cooperative sensing of mitochondrial DNA by ZBP1 and cGAS promotes cardiotoxicity. *Cell* **186**, 3031–3032 (2023).
35. J. Maelfait, J. Rehwinkel, The Z-nucleic acid sensor ZBP1 in health and disease. *J. Exp. Med.* **220**, e20221156 (2023).
36. A. Takaoka, Z. Wang, M. K. Choi, H. Yanai, H. Negishi, T. Ban, Y. Lu, M. Miyagishi, T. Kodama, K. Honda, Y. Ohba, T. Taniguchi, DAI (DLM-1/ZBP1) is a cytosolic DNA sensor and an activator of innate immune response. *Nature* **448**, 501–505 (2007).
37. N. W. Hubbard, J. M. Ames, M. Maurano, L. H. Chu, K. Y. Somfleth, N. S. Gokhale, M. Werner, J. M. Snyder, K. Lichauco, R. Savan, D. B. Stetson, A. Oberst, ADAR1 mutation causes ZBP1-dependent immunopathology. *Nature* **607**, 769–775 (2022).
38. A. Herbert, Z-DNA and Z-RNA in human disease. *Commun. Biol.* **2**, 7 (2019).
39. H. Jiao, L. Wachsmuth, S. Kumari, R. Schwarzer, J. Lin, R. O. Eren, A. Fisher, R. Lane, G. R. Young, G. Kassiotis, W. J. Kaiser, M. Pasparakis, Z-nucleic-acid sensing triggers ZBP1-dependent necroptosis and inflammation. *Nature* **580**, 391–395 (2020).
40. J. Wang, S. Wang, C. Zhong, T. Tian, X. Zhou, Novel insights into a major DNA oxidative lesion: its effects on Z-DNA stabilization. *Org. Biomol. Chem.* **13**, 8996–8999 (2015).
41. J. Saada, R. J. McAuley, M. Marcatti, T. Z. Tang, M. Motamedi, B. Szczesny, Oxidative stress induces Z-DNA-binding protein 1-dependent activation of microglia via mtDNA released from retinal pigment epithelial cells. *J. Biol. Chem.* **298**, 101523 (2022).
42. N. Li, K. Ragheb, G. Lawler, J. Sturgis, B. Rajwa, J. A. Melendez, J. P. Robinson, Mitochondrial complex I inhibitor rotenone induces apoptosis through enhancing mitochondrial reactive oxygen species production. *J. Biol. Chem.* **278**, 8516–8525 (2003).
43. L. Lama, C. Adura, W. Xie, D. Tomita, T. Kamei, V. Kuryavyi, T. Gogakos, J. I. Steinberg, M. Miller, L. Ramos-Espiritu, Y. Asano, S. Hashizume, J. Aida, T. Imaeda, R. Okamoto, A. J. Jennings, M. Michino, T. Kuroita, A. Stamford, P. Gao, P. Meinke, J. F. Glickman, D. J. Patel, T. Tuschl, Development of human cGAS-specific small-molecule inhibitors for repression of dsDNA-triggered interferon expression. *Nat. Commun.* **10**, 2261 (2019).
44. J. Cadet, A. Grand, T. Douki, "Solar UV radiation-induced DNA bipyrimidine photoproducts: Formation and mechanistic insights," in *Photoinduced Phenomena in Nucleic Acids II: DNA Fragments and Phenomenological Aspects*, M. Barbatti, A. C. Borin, S. Ullrich, Eds. (Springer International Publishing, 2014), pp. 249–275.
45. K. J. Mackenzie, P. Carroll, C. A. Martin, O. Murina, A. Fluteau, D. J. Simpson, N. Olova, H. Sutcliffe, J. K. Rainger, A. Leitch, R. T. Osborn, A. P. Wheeler, M. Nowotny, N. Gilbert, T. Chandra, M. A. M. Reijns, A. P. Jackson, cGAS surveillance of micronuclei links genome instability to innate immunity. *Nature* **548**, 461–465 (2017).
46. J. B. Chaires, Allosteric conversion of Z DNA to an intercalated right-handed conformation by daunomycin. *J. Biol. Chem.* **261**, 8899–8907 (1986).
47. F. M. Pohl, T. M. Jovin, Salt-induced co-operative conformational change of a synthetic DNA: Equilibrium and kinetic studies with poly(dG-dC). *J. Mol. Biol.* **67**, 375–396 (1972).
48. J. R. Buzzo, A. Devaraj, E. S. Gloag, J. A. Jurcisek, F. Robledo-Avila, T. Kesler, K. Wilbanks, L. Mashburn-Warren, S. Balu, J. Wickham, L. A. Novotny, P. Stoodley, L. O. Bakaletz, S. D. Goodman, Z-form extracellular DNA is a structural component of the bacterial biofilm matrix. *Cell* **184**, 5740–5758.e17 (2021).
49. Y. Zhang, Y. Cui, R. An, X. Liang, Q. Li, H. Wang, H. Wang, Y. Fan, P. Dong, J. Li, K. Cheng, W. Wang, S. Wang, G. Wang, C. Xue, M. Komiyama, Topologically constrained formation of stable Z-DNA from normal sequence under physiological conditions. *J. Am. Chem. Soc.* **141**, 7758–7764 (2019).
50. M. I. Love, W. Huber, S. Anders, Moderated estimation of fold change and dispersion for RNA-seq data with DESeq2. *Genome Biol.* **15**, 550 (2014).
51. A. Sample, Y. Y. He, Autophagy in UV damage response. *Photochem. Photobiol.* **93**, 943–955 (2017).
52. S. Lee, R. Karki, Y. Wang, L. N. Nguyen, R. C. Kalathur, T. D. Kanneganti, AIM2 forms a complex with pyrin and ZBP1 to drive PANoptosis and host defence. *Nature* **597**, 415–419 (2021).
53. S. N. Loftus, M. Gharaee-Kermani, B. Xu, T. M. Moore, A. Hannoudi, M. J. Mallbris, B. Klein, J. E. Gudjonsson, J. M. Kahlenberg, Interferon alpha promotes caspase-8 dependent ultraviolet light-mediated keratinocyte apoptosis via interferon regulatory factor 1. *Front. Immunol.* **15**, 1384606 (2024).
54. J. Kim, R. Gupta, L. P. Blanco, S. Yang, A. Shteinfer-Kuzmine, K. Wang, J. Zhu, H. E. Yoon, X. Wang, M. Kerkhofs, H. Kang, A. L. Brown, S. J. Park, X. Xu, E. Zandee van Rilland, M. K. Kim, J. I. Cohen, M. J. Kaplan, V. Shoshan-Barmatz, J. H. Chung, VDAC oligomers form mitochondrial pores to release mtDNA fragments and promote lupus-like disease. *Science* **366**, 1531–1536 (2019).
55. Y. Huang, D. D. Yang, X. Y. Li, D. L. Fang, W. J. Zhou, ZBP1 is a significant pyroptosis regulator for systemic lupus erythematosus. *Ann. Transl. Med.* **9**, 1773 (2021).

Downloaded from https://www.science.org at University of Michigan Ann Arbor on March 07, 2025

56. S. Caielli, Z. Wan, V. Pascual, Systemic lupus erythematosus pathogenesis: Interferon and beyond. *Annu. Rev. Immunol.* **41**, 533–560 (2023).
57. D. M. Spencer, E. Svenungsson, I. Gunnarsson, R. Caricchio, D. S. Pisetsky, The expression of antibodies to Z-DNA in the blood of patients with systemic lupus erythematosus: Relationship to autoantibodies to B-DNA. *Clin. Immunol.* **255**, 109763 (2023).
58. E. M. Lafer, R. P. Valle, A. Möller, A. Nordheim, P. H. Schur, A. Rich, B. D. Stollar, Z-DNA-specific antibodies in human systemic lupus erythematosus. *J. Clin. Invest.* **71**, 314–321 (1983).
59. E. Erdal, S. Haider, J. Rehwinkel, A. L. Harris, P. J. McHugh, A prosurvival DNA damage-induced cytoplasmic interferon response is mediated by end resection factors and is limited by Trex1. *Genes Dev.* **31**, 353–369 (2017).
60. C. Wolf, A. Rapp, N. Berndt, W. Staroske, M. Schuster, M. Dobrick-Mattheuer, S. Kretschmer, N. König, T. Kurth, D. Wieczorek, K. Kast, M. C. Cardoso, C. Günther, M. A. Lee-Kirsch, RPA and Rad51 constitute a cell intrinsic mechanism to protect the cytosol from self DNA. *Nat. Commun.* **7**, 11752 (2016).
61. S. Glück, B. Guey, M. F. Gulen, K. Wolter, T. W. Kang, N. A. Schmacke, A. Bridgeman, J. Rehwinkel, L. Zender, A. Ablasser, Innate immune sensing of cytosolic chromatin fragments through cGAS promotes senescence. *Nat. Cell Biol.* **19**, 1061–1070 (2017).
62. M. Gratia, M. P. Rodero, C. Conrad, E. Bou Samra, M. Maurin, G. I. Rice, D. Duffy, P. Revy, F. Petit, R. C. Dale, Y. J. Crow, M. Amor-Gueret, N. Manel, Bloom syndrome protein restrains innate immune sensing of micronuclei by cGAS. *J. Exp. Med.* **216**, 1199–1213 (2019).
63. Q. Yu, Y. V. Katlinskaya, C. J. Carbone, B. Zhao, K. V. Katlinski, H. Zheng, M. Guha, N. Li, Q. Chen, T. Yang, C. J. Lengner, R. A. Greenberg, F. B. Johnson, S. Y. Fuchs, DNA-damage-induced type I interferon promotes senescence and inhibits stem cell function. *Cell Rep.* **11**, 785–797 (2015).
64. A. G. Singh, C. S. Crowson, S. Singh, M. D. P. Davis, H. Maradit-Kremers, E. L. Matteson, V. R. Chowdhary, Cancer risk in cutaneous lupus erythematosus: a population-based cohort study. *Rheumatology* **55**, 2009–2013 (2016).
65. M. A. Sherwani, I. Ahmad, M. J. Lewis, A. Abdelgawad, H. Rashid, K. Yang, C. Y. Chen, C. Raman, C. A. Elmets, N. Yusuf, Type I interferons enhance the repair of ultraviolet radiation-induced DNA damage and regulate cutaneous immune suppression. *Int. J. Mol. Sci.* **23**, 1822 (2022).
66. H. He, L. Xiong, L. Jian, L. Li, Y. Wu, S. Qiao, Role of mitochondria on UV-induced skin damage and molecular mechanisms of active chemical compounds targeting mitochondria. *J. Photochem. Photobiol. B Biol.* **232**, 112464 (2022).
67. H. Jiao, L. Wachsmuth, S. Wolf, J. Lohmann, M. Nagata, G. G. Kaya, N. Oikonomou, V. Kondylis, M. Rogg, M. Diebold, S. E. Troder, B. Zevnik, M. Prinz, C. Schell, G. R. Young, G. Kassiotis, M. Pasparakis, ADAR1 averts fatal type I interferon induction by ZBP1. *Nature* **607**, 776–783 (2022).
68. T. Zhang, C. Yin, A. Fedorov, L. Qiao, H. Bao, N. Beknazarov, S. Wang, A. Gautam, R. M. Williams, J. C. Crawford, S. Peri, V. Studitsky, A. A. Beg, P. G. Thomas, C. Walkley, Y. Xu, M. Poptsova, A. Herbert, S. Balachandran, ADAR1 masks the cancer immunotherapeutic promise of ZBP1-driven necroptosis. *Nature* **606**, 594–602 (2022).
69. R. de Reuver, S. Verdonck, E. Dierick, J. Nemegeer, E. Hessmann, S. Ahmad, M. Jans, G. Blancke, F. Van Nieuwerburgh, A. Botzki, L. Vereecke, G. van Loo, W. Declercq, S. Hur, P. Vandenabeele, J. Maelfait, ADAR1 prevents autoinflammation by suppressing spontaneous ZBP1 activation. *Nature* **607**, 784–789 (2022).
70. M. Devos, G. Tanghe, B. Gilbert, E. Dierick, M. Verheirstraeten, J. Nemegeer, R. de Reuver, S. Lefebvre, J. De Munck, J. Rehwinkel, P. Vandenabeele, W. Declercq, J. Maelfait, Sensing of endogenous nucleic acids by ZBP1 induces keratinocyte necroptosis and skin inflammation. *J. Exp. Med.* **217**, e20191913 (2020).
71. L. Freund, S. Oehrl, J. Schwingen, S. Haeberle, T. Döbel, P. D. H. Lee, S. Meisel, S. Mihalceanu, M. Rußwurm, T. Luft, K. Schäkel, IFNγ causes keratinocyte necroptosis in acute graft-versus-host disease. *J. Invest. Dermatol.* **143**, 1746–1756.e9 (2023).
72. D. M. Bissell, K. E. Anderson, H. L. Bonkovsky, Porphyria. *N. Engl. J. Med.* **377**, 862–872 (2017).
73. A. D'Urso, A. Mammana, M. Balaz, A. E. Holmes, N. Berova, R. Lauceri, R. Purrello, Interactions of a tetraanionic porphyrin with DNA: From a Z-DNA sensor to a versatile supramolecular device. *J. Am. Chem. Soc.* **131**, 2046–2047 (2009).
74. M. A. Dickson, W. C. Hahn, Y. Ino, V. Ronfard, J. Y. Wu, R. A. Weinberg, D. N. Louis, F. P. Li, J. G. Rheinwald, Human keratinocytes that express hTERT and also bypass a p16INK4a-enforced mechanism that limits life span become immortal yet retain normal growth and differentiation characteristics. *Mol. Cell. Biol.* **20**, 1436–1447 (2000).
75. M. K. Sarkar, R. Uppala, C. Zeng, A. C. Billi, L. C. Tsoi, A. Kidder, X. Xing, B. E. Perez White, S. Shao, O. Plazyo, S. Sirobhushanam, E. Xing, Y. Jiang, K. A. Gallagher, J. J. Voorhees, J. M. Kahlenberg, J. E. Gudjonsson, Keratinocytes sense and eliminate CRISPR DNA through STING/IFN-κ activation and APOBEC3G induction. *J. Clin. Invest.* **133**, e159393 (2023).
76. B. Xu, I. Gerin, H. Miao, D. Vu-Phan, C. N. Johnson, R. Xu, X.-W. Chen, W. P. Cawthorn, O. A. MacDougald, R. J. Koenig, Multiple roles for the non-coding RNA SRA in regulation of adipogenesis and insulin sensitivity. *PLOS ONE* **5**, e14199 (2010).
77. J. D. Bryant, Y. Lei, J. J. VanPortfliet, A. D. Winters, A. P. West, Assessing mitochondrial DNA release into the cytosol and subsequent activation of innate immune-related pathways in mammalian cells. *Curr. Protoc.* **2**, e372 (2022).
78. C. C. Berthier, L. C. Tsoi, T. J. Reed, J. N. Stannard, E. M. Myers, R. Namas, X. Xing, S. Lazar, L. Lowe, M. Kretzler, J. E. Gudjonsson, J. M. Kahlenberg, Molecular profiling of cutaneous lupus lesions identifies subgroups distinct from clinical phenotypes. *J. Clin. Med.* **8**, 1244 (2019).
79. J. L. Turnier, L. M. Pachman, L. Lowe, L. C. Tsoi, S. Elhaj, R. Menon, M. C. Amoruso, G. A. Morgan, J. E. Gudjonsson, C. C. Berthier, J. M. Kahlenberg, Comparison of lesional juvenile myositis and lupus skin reveals overlapping yet unique disease pathophysiology. *Arthritis Rheumatol.* **73**, 1062–1072 (2021).
80. V. G. Tusher, R. Tibshirani, G. Chu, Significance analysis of microarrays applied to the ionizing radiation response. *Proc. Natl. Acad. Sci. U.S.A.* **98**, 5116–5121 (2001).
81. X. Feng, H. Wu, J. M. Grossman, P. Hanvivadhanakul, J. D. FitzGerald, G. S. Park, X. Dong, W. Chen, M. H. Kim, H. H. Weng, D. E. Furst, A. Gorn, M. McMahon, M. Taylor, E. Brahn, B. H. Hahn, B. P. Tsao, Association of increased interferon-inducible gene expression with disease activity and lupus nephritis in patients with systemic lupus erythematosus. *Arthritis Rheum* **54**, 2951–2962 (2006).
82. R. Patro, G. Duggal, M. I. Love, R. A. Irizarry, C. Kingsford, Salmon provides fast and bias-aware quantification of transcript expression. *Nat. Methods* **14**, 417–419 (2017).

Acknowledgments: We thank the patients for their participation in this study. We thank S. Yalavarthi for helpful technical assistance. We acknowledge the assistance of the microscopy core and the advanced genomics core at the University of Michigan. We thank J. Sexton for use of the Cell Voyager 8000 (CV8000, Yokogawa) automated dual microlens spinning disk confocal microscope. We thank J. Whitfield in the Rogel Cancer Center Immunology core for the ELISA analysis. The U-M Advanced Research Computing Great Lakes computing cluster was used for high-content image analysis. **Funding:** This work was supported by the National Institutes of Health (NIH) through award nos. R01AR071384, K24AR076975, R03AR066337 (to J.M.K.), P30AR075043 (to J.E.G.), R01AI157384 (to M.O.R.), and K23AR080789 (to J.L.T.), the German Research Foundation fund KL3612/1-1 (to B.K.), the Rheumatology Research Foundation Investigator Award 025850 (to J.L.T.), Cure JM Award Michigan12/20 (to J.L.T.), the University of Michigan Immunology Program Research Training in Experimental Immunology training grant T32 AI007413 (to M.R.), the Miller Fund Award for Innovative Immunology Research (to M.R.), the American Heart Association and Barth Syndrome Foundation cofunded predoctoral fellowship 23PRE1019408 (to M.R.), the George M. O'Brien Michigan Kidney Translational Resource Center (MKTC) NIH/National Institute of Diabetes and Digestive and Kidney Diseases (NIDDK) grant U54DK137314 (to C.B.), and the Taubman Institute Innovative Programs (to J.M.K. and J.E.G.). **Author contributions:** Conceptualization: B.K. and M.K. Methodology: B.K., M.R., B.X., M.G.K., C.B., S.H., S.E., J.E.G., K.E.M., A.V., C.D., M.O.R., and J.M.K. Investigation: B.K., M.R., B.X., M.G.K., Y.G., C.B., A.V., S.E., S.H., L.T., C.D., G.H., F.M., J.T., J.E.G., M.O.R., and J.M.K. funding acquisition: B.K., M.R., M.O.R., and M.K. Visualization: B.K., M.R., B.X., M.G.K., C.B., and S.H. Project administration: M.K. Supervision: J.E.G., M.O.R., and J.M.K. Writing—original draft: B.K. and K.M. Writing—review and editing: B.K., M.R., J.T., J.E.G., M.O.R., and J.M.K. **Competing interests:** J.M.K. has received grant support from Q32 Bio, Celgene/Bristol-Myers Squibb, Ventus Therapeutics, Rome Therapeutics, and Janssen. J.M.K. has served on advisory boards for AstraZeneca, Biogen, Bristol-Myers Squibb, Eli Lilly, EMD serrano, Exo Therapeutics, Gilead, GlaxoSmithKline, Aurinia Pharmaceuticals, Rome Therapeutics, Synthekine, Vivideon, and Ventus Therapeutics. J.E.G. has received support from Eli Lilly, Janssen, BMS, Sanofi, Prometheus, Almirall, Kyowa-Kirin, Novartis, AnaptysBio, Boehringer Ingelheim, Regeneron, AbbVie, and Galderma. **Data and materials availability:** Skin wide-genome expression datasets are publicly available for CLE through GEO GSE81071, for adult DM through GSE142807, and for cSLE and JDM through GEO GSE148810. The single-cell RNA sequencing data are available in GEO under accession number GSE186476. Pipelines for automated image analysis in CellProfiler are within the supplementary files of this manuscript. Knockout cell lines are available through the U-M Skin Biology and Diseases Resource Center Functional Analytics Core (https://medresearch.umich.edu/labs-departments/centers/skin-research/research/core-services/functional-analytics-core). All other data supporting the conclusions of the manuscript including patient data are available in the main text or the Supplementary Materials.

Submitted 22 January 2024
Resubmitted 14 November 2024
Accepted 11 February 2025
Published 7 March 2025
10.1126/sciimmunol.ado1710

Downloaded from https://www.science.org at University of Michigan Ann Arbor on March 07, 2025